BRNO UNIVERSITY OF TECHNOLOGY

Faculty of Electrical Engineering and Communication

MASTER'S THESIS

Brno, 2022　　　　　　　　　　　　　　Bc. Josef Laštovička

BRNO UNIVERSITY OF TECHNOLOGY

VYSOKÉ UČENÍ TECHNICKÉ V BRNĚ

FACULTY OF ELECTRICAL ENGINEERING AND COMMUNICATION

FAKULTA ELEKTROTECHNIKY
A KOMUNIKAČNÍCH TECHNOLOGIÍ

DEPARTMENT OF POWER ELECTRICAL AND ELECTRONIC ENGINEERING

ÚSTAV VÝKONOVÉ ELEKTROTECHNIKY A ELEKTRONIKY

THE OPTIMUM SUPPLY OF A WOUND-ROTOR SYNCHRONOUS MACHINE WITH RESPECT TO MAXIMUM EFFICIENCY

OPTIMÁLNÍ NAPÁJENÍ SYNCHRONNÍHO STROJE S VINUTÝM ROTOREM S OHLEDEM NA MAX. ÚČINNOST

MASTER'S THESIS

DIPLOMOVÁ PRÁCE

AUTHOR   Bc. Josef Laštovička
AUTOR PRÁCE

SUPERVISOR   Ing. Jan Bárta, Ph.D.
VEDOUCÍ PRÁCE

BRNO 2022

BRNO FACULTY OF ELECTRICAL
UNIVERSITY ENGINEERING
OF TECHNOLOGY AND COMMUNICATION

Master's Thesis

Master's study program **Power Electrical and Electronic Engineering**

Department of Power Electrical and Electronic Engineering

Student:	Bc. Josef Laštovička	**ID:**	203277
Year of study:	2	**Academic year:**	2021/22

TITLE OF THESIS:

The optimum supply of a wound-rotor synchronous machine with respect to maximum efficiency

INSTRUCTION:

1. Conduct and write a literature review on the traction applications of wound rotor synchronous machines.
2. Describe the methods of analysis and evaluation of the operating characteristics of a wound rotor synchronous machine.
3. Develop code for analysis of the operating characteristics of a wound rotor synchronous machine and searching for an optimal combination of stator and excitation currents for selected conditions.
4. Verify developed methodology on selected wound field synchronous machine.

The work is carried out in collaboration with JKU - Johannes Kepler Universität Linz and the LCM - Linz Center of Mechatronics.

RECOMMENDED LITERATURE:

[1] P. C. Sen: Principles of Electric Machines and Power Electronics, ISBN: 9781118078877 (EN)

[2] Juha Pyrhonen , Valeria Hrabovcova , R. Scott Semken: Electrical Machine Drives Control : An Introduction, ISBN: 9781119260455 (EN)

[3] G. Weidenholzer, S. Silber, G. Jungmayr, G. Bramerdorfer, H. Grabner and W. Amrhein, "A flux-based PMSM motor model using RBF interpolation for time-stepping simulations," 2013 International Electric Machines & Drives Conference, 2013, pp. 1418-1423, doi: 10.1109/IEMDC.2013.6556323.

Date of project specification:	7.2.2022	**Deadline for submission:**	22.5.2022

Supervisor: Ing. Jan Bárta, Ph.D.
Consultant: Assoz. Univ. Prof. DI Dr. Gerd Bramerdorfer

doc. Ing. Ondřej Vítek, Ph.D.
Chair of study program board

ABSTRACT

The master's thesis deals with a literature review of electric motors suitable for the electric vehicle driveline, where the main focus is given to a wound-field synchronous machine. At first, there is a short description of machine construction and the working principle for each type of suitable electric machine. The advantages and disadvantages of using a specific machine as a traction drive are summarized, and an eventual example of use in today's electric car with basic machine specifications is given. In the next part, a more detailed focus is given to the wound-rotor synchronous machine and its use for electric vehicle drive. The second chapter deals with the modification of this machine type for traction applications. A machine capable of dual-mode operation is presented, followed by a discussion of non-contact current transfer to the rotor winding, and finally, the possibility of using a hairpin winding made of rectangular conductors is presented. The third part of the thesis deals with the mathematical description of the machine, including direct and quadrature axis equivalent circuits and an explanation of the vector diagram in motor mode. In the last two chapters of the thesis, a Python program is introduced to analyze the machine's operating characteristics. During the program build, an analysis methodology for this type of machine based on the provided data package was developed, and graphical dependencies of torque and efficiency on different input currents combinations were exported. The program also includes a function for finding the optimum current supply for the machine with respect to the maximum efficiency.

KEYWORDS

Electric car, Machine comparison, Synchronous machine, Wound-field machine, Traction machine, Salient pole, Machine modifications, Mathematical model, Python, Analysis

ABSTRAKT

Tato diplomová práce se zabývá literární rešerší elektromotorů, které je možné použít pro pohon elektrických vozidel, přičemž hlavní pozornost je věnována strojům s vinutým rotorem. Na začátek je proveden krátký popis konstrukce a principu činnosti každého vhodného typu elektrického stroje. Jsou zde shrnuty výhody a nevýhody použití stroje jako trakčního pohonu a případné použití v dnešním elektromobilu včetně základních specifikací. Dále je věnován detailnější pohled na stroj s vinutým rotorem a jeho použití pro pohon elektrických vozidel. Následná část práce se věnuje úpravám tohoto typu stroje pro použití v trakčních aplikacích. Je zde představen stroj, který je schopen provozu ve dvou módech, následně je diskutován bezkontaktní přenos proudu do rotorového vinutí a nakonec je představena možnost použití tvarovaného vinutí z vodičů obdélníkového průřezu. Předposlední část práce se zabývá matematickým popisem stroje včetně náhradních schémat v podélné a příčné ose a vysvětlením vektorového diagramu v motorickém režimu. V posledních dvou kapitolách práce je představen program v jazyce Python, který slouží k analýze provozních charakteristik stroje. V rámci práce na programu byla vytvořena metodika analýzy tohoto typu stroje na základě poskytnutého balíčku dat. Dále byly vyexportovány grafické závislosti momentu a účinnosti na různých kombinacích vstupních proudů. Součástí programu je také funkce pro hledání optimálního napájení stroje s ohledem na nejvyšší účinnost.

KLÍČOVÁ SLOVA

Elektromobil, Porovnání strojů, Synchronní stroje, Stroj s vinutým rotorem, Trakční motor, Vyniklé póly, Úpravy stroje, Matematický model, Python, Analýza

ROZŠÍŘENÝ ABSTRAKT

Tato práce se zabývá využitím synchronního stroje s vinutým rotorem pro pohon elektrických vozidel a porovnáním s ostatními používanými pohony. V první části byla tedy provedena literární rešerše motorů, které by bylo možné použít pro trakční pohon. Bylo nalezeno pět používaných typů motorů. Pro každý typ motoru byla stručně popsána jeho konstrukce, princip činnosti a byly shrnuty výhody a nevýhody pro trakční použití.

Prvním z nich byl stejnosměrný motor, který nabízí jednoduché řízení a známou koncepci. Velikou nevýhodou je však použití komutátoru, který vyžaduje častou údržbu a vytváří značné znečištění okolních součástí pohonu. Z toho důvodu se v dnešní době nepoužívá k pohonu větších elektrických vozidel. Druhým typem byl synchronní motor s permanentními magnety. Na základě rešerše bylo zjištěno, že tento motor je hojně používaný v dnešních elektromobilech. Je to z důvodu jeho velkého výkonu na malý objem a vysokého záběrného momentu. Nevýhodou tohoto stroje je poměrně strmě vzrůstající cena magnetů vyrobených ze vzácných zemin, proto je snaha hledat bezmagnetová řešení elektrického pohonu vozidel. Nejjednodušší bezmagnetový typ stroje je reluktanční motor, kde na rotoru není umístěno žádné vinutí ani magnety. Motor využívá principu změny reluktance magnetického obvodu, která má za následek snižování magnetického odporu na nejmenší možnou hodnotu. Velikou výhodou tohoto stroje je jeho nízká pořizovací cena a robustní konstrukce, nevýhodou však jsou poměrně velké vibrace a hluk. Proto se v soušasné době vyvíjí řídící algoritmus, který by tyto nevýhody minimalizoval. Dobře známým a používaným typem stroje je rovněž asynchronní motor. Díky jeho jednoduché konstrukci a poměrně snadné výrobě je levný. Pro použití do elektromobilu však musí být mírně upraven, což zvyšuje jeho cenu. Velmi pokročilý vývoj asynchronního stroje se podařil firmě Tesla, která tento typ stroje používá v některých modelech elektromobilů. Výhodou tohoto stroje je jednoduchá a odolná kostrukce a poměrně levná cena oproti strojům s permanentními magnety, nevýhodou pak mírně nižší účinnost a potřeba vytvářet v měniči jalový proud, který je potřebný pro buzení stroje, což zvyšuje hodnotu proudového dimenzování spínacích prvků.

Posledním typem motoru, který nepoužívá permanentní magnety je synchronní stroj s vinutým rotorem. Tomuto stroji byla věnována detailnější pozornost. Byla popsána jeho konstrukce, typy rotorů a princip činnosti. Byly diskutovány výhody a nevýhody při trakčním použití. Velkou výhodou je možnost měnit budicí proud za chodu motoru, což umožňuje odbuzování stroje ve vysokých otáčkách. Nevýhodou je mírně nižší účinnost oproti strojům s permanentními magnety.

V rámci literární rešerše na téma synchronních strojů s vinutým rotorem pro trakční aplikace byly do této práce umístěny i úpravy, jež se na těchto strojích

provádí. V rámci práce byl tedy popsán princip činnosti stroje, který je schopen pracovat ve vernier režimu. Dále byly probrány dvě metody bezkontaktního přenosu proudu do statorového vinutí. První z nich byl rotační transformátor, který využívá jádro vyrobené z kompozitních materiálů, čímž se významně snižuje jeho objem. Následně byl představen koncept kapacitního přenosu energie, jehož největší výhodou je velmi malý objem. Poslední představenou úpravou bylo použití tvarovaného vinutí společně s vodiči statoru, jež mají obdélníkový tvar.

V další kapitole byl popsán model synchronního stroje s vinutým rotorem pomocí ekvivalentních obvodů v přímé i příčné ose. Z těchto schémat vycházeli sepsané matematické rovnice, podle nichž bylo možné stroj namodelovat. V rámci matematického popisu byla uvedena i rovnice pro výpočet točivého momentu, kde byl vysvětlen význam jednotlivých částí této rovnice. Pro ucelení matematického popisu byl vložen a vysvětlen i vektorový diagram stroje v motorickém režimu.

Dále je ve čtvrté kapitole popsána spolupráce s Univerzitou Johanesse Keplera v Linci, která poskytla data k analýze stroje. Nejprve byla vytvořena tréninková data, která sloužila k vytvoření skriptu v programovacím jazyce Python. V této kapitole byly tedy prezentovány dílčí výsledky a metodika analýzy provozních charakteristik synchronního stroje s vinutým rotorem. Jelikož však data měla omezený rozsah v generátorickém režimu, bylo třeba ověřit funkčnost skriptu na jiném stroji.

V páté kapitole jsou tedy prezentovány výsledky analýzy synchronního stroje, který byl navržen přímo na Institutu elektrických pohonů a výkonové elektroniky na JKU v Linzi. Tento stroj byl navržen právě jako trakční pohon elektromobilu. Z výsledků analýzy byly vytvořeny momentové a účinnostní charakteristiky. V rámci skriptu je také nalezena hodnota nejvyšší účinnosti a korespondující napájecí proudy, které byly potřeba k jejímu dosažení. Tato kombinace proudů může být následně použita pro optimální napájení daného synchronního stroje s vinutým rotorem.

Author's Declaration

Author:	Bc. Josef Laštovička
Author's ID:	203277
Paper type:	Master's Thesis
Academic year:	2021/22
Topic:	The optimum supply of a wound-rotor synchronous machine with respect to maximum efficiency

I declare that I have written this paper independently, under the guidance of the advisor and using exclusively the technical references and other sources of information cited in the paper and listed in the comprehensive bibliography at the end of the paper.

As the author, I furthermore declare that, with respect to the creation of this paper, I have not infringed any copyright or violated anyone's personal and/or ownership rights. In this context, I am fully aware of the consequences of breaking Regulation § 11 of the Copyright Act No. 121/2000 Coll. of the Czech Republic, as amended, and of any breach of rights related to intellectual property or introduced within amendments to relevant Acts such as the Intellectual Property Act or the Criminal Code, Act No. 40/2009 Coll. of the Czech Republic, Section 2, Head VI, Part 4.

Brno ....

....

author's signature*

---

*The author signs only in the printed version.

ACKNOWLEDGEMENT

Contents

List of Figures

List of Tables

Introduction

Nowadays, the automotive industry is at the beginning of a massive transformation due to climate change and the subsequent demands of governments around the world. This transformation is based on the transition from internal combustion engines to an electric drive system for daily used cars. This change brings many opportunities to develop a suitable electric drive, so this thesis deals with literature research on possible solutions for electric vehicle driveline, their modifications for this application, and the analysis of the operating characteristics of a selected wound-rotor synchronous machine.

The first chapter is focused on literature research on traction motors used in electric vehicles. To better understand machine behavior, the construction and working principle of each type is discussed. The advantages and disadvantages of these machine types are summarized to determine the best choice and compare all machines properly. The wound-field synchronous machine has significant potential as an electric vehicle motor due to the rising price of rare-earth materials.

The second chapter deals with modifying a wound rotor synchronous machine for use in traction applications. Two operation modes of the vernier machine are presented. Since the most significant disadvantage of the wound rotor machines is the sliding contact, further attention is given to the contact-less transfer of current to the excitation winding on the rotor. The principle of power transfer using a rotary transformer and capacitor is described in this work. The last modification is the use of hairpin winding and rectangular conductors.

The mathematical analysis of the machine is carried out in the third chapter. Within this analysis, the direct and quadrature axis equivalent circuits are described. These diagrams are then used as the basis for the mathematical equations, including the torque equation, where the meaning of its parts is explained. The vector diagram described at the end of this chapter is also derived from the equivalent circuits and mathematical equations.

The last two chapters are focused on the script for machine operating characteristics analysis. The script includes data loading with the possibility of conversion from the three-phase system to the rotor reference frame if the values are not already exported from simulations using the finite element method. The calculated torque is then compared with the simulation results for the transformation verification.

Furthermore, chapter four describes the collaboration with Johannes Kepler University in Linz, which provided the data for the analysis of the machine. Firstly, training data was generated to create a script in the Python programming language. However, since the training data pack was limited in generator mode, it was necessary to verify the functionality of the script on another machine. Thus,

in this chapter, partial results and methodology for the analysis of the operating characteristics of the wound-rotor synchronous machine were presented.

Chapter five presents the results of the analysis of the synchronous machine, which was designed directly at the Institute of Electric Drives and Power Electronics at JKU in Linz. This machine was designed specifically as a traction drive. From the analysis results, the torque and efficiency characteristics were developed. The value of the highest efficiency and the corresponding supply currents needed to achieve it are also found within the script. This combination of currents can then be used to power a given synchronous machine with a wound rotor optimally.

1   Electric machines for traction applications

Traction applications of electric motors have become a big topic over the last few years as pressure to reduce passenger car emissions has forced car manufacturers to switch to hybrid or fully-electric drive. As a result, much effort has been devoted to developing the most efficient electric car drive possible. At present, machines with rare earth magnets are mainly used for this purpose. However, according to [1], the price of these magnets is increasing rapidly. That is why, according to [2], is currently looking for a way to avoid the use of rare-earth magnets. One way is to use a wound rotor synchronous machine, as described in [1].

After studying the data from articles [3] and [2], which are summarized in Fig. 1.1, it was found that most electric automobile manufacturers have been using rare-earth PM machines recently.
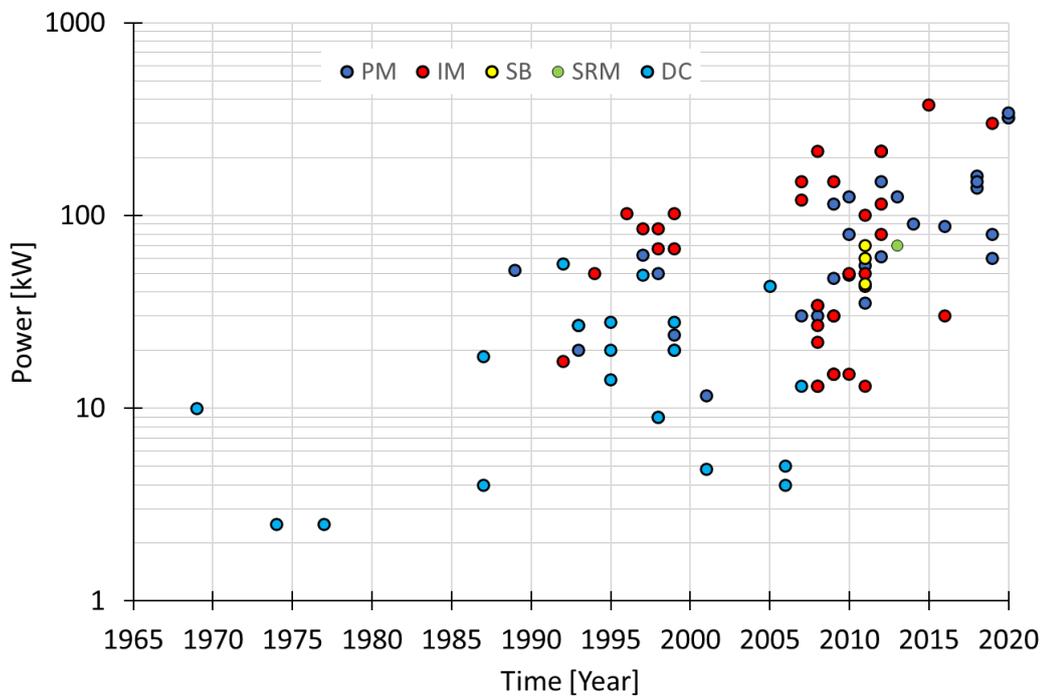
Fig. 1.1: Overview of used motors for EV driveline. PM-Permanent Magnet, IM-Induction Motor, SB-Synchronous Brushed, SRM-Synchronous Reluctance Motor, DC-Direct Current. Source data from [3] and [2].

As mentioned in [3], [4] and [5], the development of electric drive brings many specific requirements. Most of these parameters are derived from the vehicle's requirements, like acceleration, maximum speed, or wide distance range. Required parameters for the electric drive are summarized below:

- Low weight, volume and price.
- High power density.
- High starting and low speed torque.
- High efficiency over the whole wide speed range.
- Capabilities for overloading due to acceleration.
- Possibility of recuperative braking.
- Torque ripple and noise as low as possible.
- Robustness and ability to work even in case of failure.

The definition of a suitable traction motor depends on many factors. Unfortunately, most of the required properties can often be contradictory, so it is hard work to find out an acceptable compromise. Global car manufacturers have also taken different paths to achieve these requirements. The engine's chosen concept and control system plays a significant role in meeting these requirements. This section focuses on comparing the most used electric traction motor concepts in EV and HEV cars. Based on efficiency maps in Fig. 1.2, high power density and high torque should be a PM motor type the best choice.
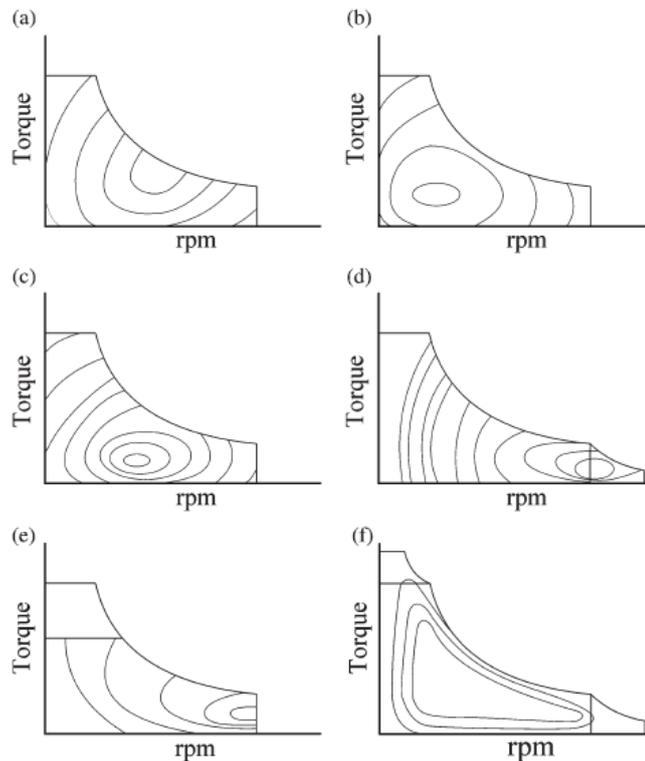
Fig. 1.2: Efficiency maps of surface mounted (a) and interior mounted PM (b) motor, induction motor (c), reluctance motor (d), DC motor (e), and synchronous motor (f). Reprinted from [3].

Data from [3] and [2], which are summarized in Fig. 1.1, say that many car producers have used PM motors recently, but there is a serious disadvantage of PM motors. It is the price of rare-earth material and its limited amount on our planet. The idea that most cars in the world will use rare-earth PM motors leads to a dramatic increase in the price of this material and, therefore, the whole car. According to [2], there is a requirement for PM-free traction motor design. This leads to using an induction motor (IM) for its simple construction or a synchronous brushed motor for its magnetic flux linkage regulation. Both of these alternative types reduce the production price and thus the vehicle's purchase price.

1.1 DC machines

The DC machine was the first machine type, which used to be a driveline of EV. As stated in [6], this machine type was used before the evolution of control electronics for AC machines.

1.1.1 Construction and principle of operation

DC machines are the oldest rotating machines. Construction and principle of operation are described in [7]. Machine operation is based on the function of a mechanical commutator. The commutator is placed at the same shaft as the machine's rotor, rotating at a similar speed. Lamellas of the commutator are slip-connected to fixed brushes, which causes a shift of rotor magnetic field perpendicular to stator magnetic field and subsequent rotation causes the conversion from the directional voltage (DC) to alternating voltage (AC). Stator magnetic field is produced by PM in the case of smaller machines or by the stator winding in the case of larger machines. The basic construction structure of the DC machine is shown in Fig. 1.3.
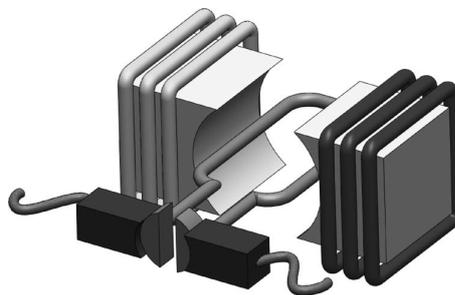
Fig. 1.3: The basic construction of the DC machine. Reprinted from [3].

1.1.2   Stator and rotor coil connection

Stator and rotor winding can be sourced separately or both from one source. There are three ways to connect stator and rotor coils when using only one source. The first option is a series motor, where stator and rotor coils are connected in series. As stated in [7], the series motor has typically high starting torque and low torque at high speed. It is suitable for high starting torque applications like trains, trams, cranes, or automobile starters. These motors must operate under load. Otherwise, they could be destroyed due to overcoming the critical speed.

The second option is to connect coils in parallel and create a shunt motor. The shunt motor is widely used for mechanical load drive. The speed of the motor can be easily controlled by armature (rotor) coil voltage at rated excitation current. Another option for speed control is to change the excitation current.

The last variation of the DC machine is a compound machine, which combines series and shunt motor together. This type is widely used for generators, where the terminal voltage needs to be constant, but the load is variable. The shunt winding is used as primary winding, and series winding compensates voltage drops across armature winding resistivity.

1.1.3   Advantages and disadvantages

The main advantages and disadvantages of DC machines in global are discussed in [6] and [8]. The most significant advantage of a brushed DC machine is the simplicity of its control. If the motor is well designed, it can be connected directly to the car battery, so there is no need to connect some complex drive electronics. Other advantages of DC machines are wide speed regulation range, robustness, low cost, linear regulating characteristics, and [9] adds to benefits possibility of high overloading. On the other hand, DC machines have a significant disadvantage too. Brushes and mechanical commutator increases the need for maintenance and decreases reliability, which is truly important for a daily used electric car. Other aspects are low efficiency and complicated construction, especially for higher output power machines.

DC motors were previously used to power electric cars, but nowadays, technologies bring other options. The trend of currently mounted machine types in EV is visible in Fig. 1.1, where most of the used engines of the last ten years are IM or PM machines. All mentioned pros and cons of DC machines led to the need to find some better driveline for nowadays EV.

1.2 Permanent magnet AC machines

Permanent magnet-based motors are the most common solution for EV and HEV drivelines. Those machines are excited by rotor-mounted permanent magnets. PM excitation replaces excitation winding, so there are no rotor copper losses, which increases efficiency. Permanent magnets are widely made of rare-earth materials, mostly NdFeB. Referring to [4] NdFeB are used at higher temperatures and provide remanent flux density up to 1.4 T. These parameters enable to design of smaller and lighter machines with high torque density and high efficiency.

Permanent magnet AC machines can be called permanent magnet synchronous machines (PMSM) and brushless DC machines (BLDC). It could seem that the BLDC machine should be classified as a DC machine, but literature [7] and [10] classify it as AC synchronous machine. This classification is due to their similar construction and non-constant input signal. The difference is only in the shape of the input power signal and, therefore rotor position sensor.

PMSM operates ideally with sinusoidal back electromotive force and is fed by a sinusoidal source. As it was said in [10], the BLDC machine has the rectangular back electromotive force and, therefore, the rectangular input current shape. In [7] is mentioned that in the case of nonideal voltage and current shape, the BLDC motor creates higher torque ripple and noise than the PMSM. Low noise and vibration, which could be caused by torque ripple, are also remembered in [11] as EV and HEV driveline criteria. So there is more suitable to use PMSM than BLDC.

1.2.1 Construction and principle of operation

The construction of the PMSM is quite simple. According to [10], there are many variations of stator and coils design, but the main goal is to achieve as much sinusoidal air gap magnetic field. Thanks to that, the stator design is similar to an induction motor or wound-rotor synchronous machine, so as with an asynchronous machine, the stator is laminated of metal sheets, and a harmonic winding is distributed in slots. As mentioned in [12], stator coils are sourced by inverter, which converts DC battery voltage to AC harmonic voltage. Motor speed is controlled by voltage frequency because the rotor has the same speed as the rotating magnetic field provided by the stator winding.

As already mentioned, the rotor of the PMSM machine provides excitation flux thanks to mounted magnets. There are many topologies of rotor magnet mounting. Some of them are shown in Fig. 1.4. These topologies can be sorted into the surface or interior mounted.
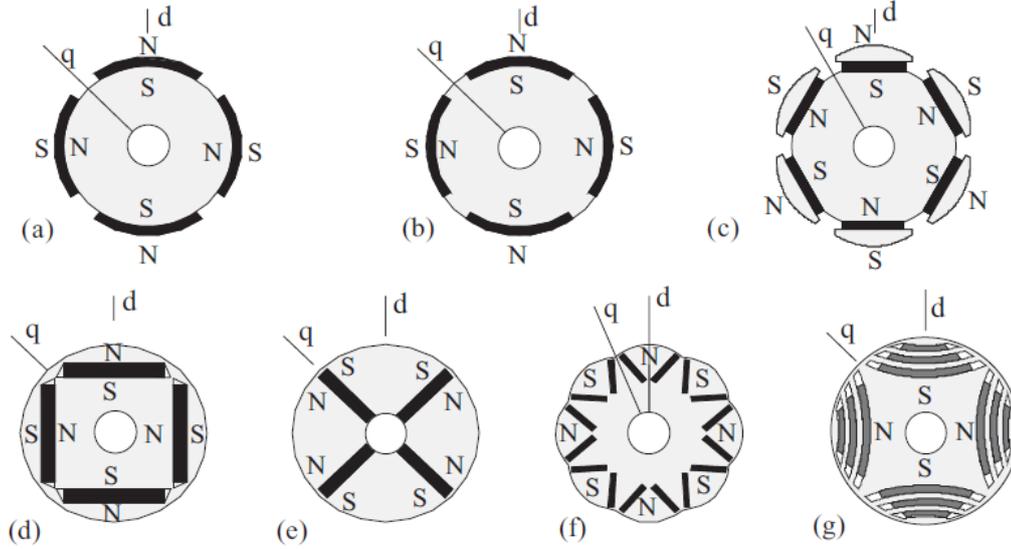
Fig. 1.4: Examples of PMSM rotor topologies, surface mounted (a) and intetior mounted (b)-(g). Reprinted from [10].

1.2.2 Surface mounted magnets

Machine with surface mounted magnets, shown in Fig. 1.4 (a), is the simplest PM machine. With refer to [7], this rotor type is widely used in servo drives, fans, and robotics thanks to its low moment of inertia and simple construction. The rotor can be made of solid or laminated steel. Used magnets are radially magnetized and glued to the rotor surface. There is a need to bandage magnets for mechanical safety in higher-speed applications. Due to PM's relative permeability near to relative air permeability, the rotor is magnetically nonsalient, so the direct and quadrature axis inductances are similar. The [10] adds that this machine type has the best utilization of PM material. However, as the magnets are on the surface, close to the stator magnetic field, there is a high risk of demagnetization. Also, the cogging torque rises.

1.2.3 Interior mounted magnets

Interior mounted magnets are embedded in the rotor steel. According to [7], this construction brings more safety solutions in terms of the mechanical forces and creates reluctance torque due to different q-axis and d-axis inductances, which adds to the torque produced by magnets.

The PMSM with magnets inset under the rotor surface is visualized in Fig. 1.4 (b). This construction is close to surface mounted, but as mentioned upper, it

creates reluctance torque and is safer. Applications are similar to surface mounted rotors.

Rotors visualised in Fig. 1.4 (d)-(f) are most common interior mounted PM machines. In [7] is mentioned that their high torque and secure magnets placement predestines them for the EV drive application. For an example of motor construction in a commercial vehicle, a Nissan LEAF (2012) was chosen. In [13] the design of the Nissan LEAF motor was investigated. Motor parameters are summarized in Tab. 1.1.

Tab. 1.1: Nissan LEAF motor parameters.

Parameter	Value	Unit
Power	80	kW
Number of poles	8	-
Speed rating	10 390	rpm
Peak torque	280	Nm
Stator outer diameter	198	mm
Rotor outer diameter	130	mm
Stack length	151	mm

Nissan LEAF is, in consonance with [4], ranked as the best-selling pure EV. A very low-weight motor with low noise and vibrations was designed thanks to magnetic circuit optimization. Optimized geometry of one rotor pole with flux lines under load is shown in Fig. 1.5.
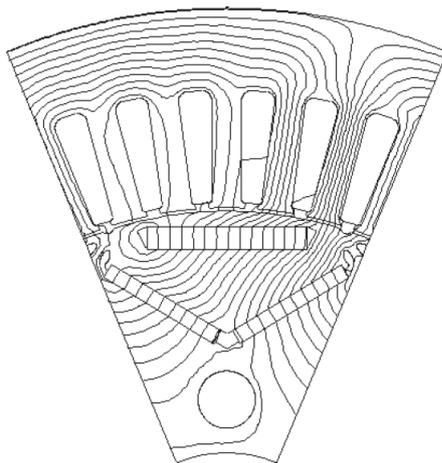
Fig. 1.5: Nissan LEAF one rotor pole geometry with flux lines under load. Reprinted from [4].

Complete motor body of water-cooled 80kW interior magnets PMSM with maximum torque 280 Nm and speed rating 10 390 rpm is photographed in Fig. 1.6. The mass of the whole motor body is about 56 kg.

Fig. 1.6: Nissan LEAF complete motor body. Reprinted from [13].

The stator of the machine with the phase connection clips is shown in Fig. 1.7 and the rotor is shown in Fig. 1.8. According to [4], the material for permanent magnets is NdDyFeB.
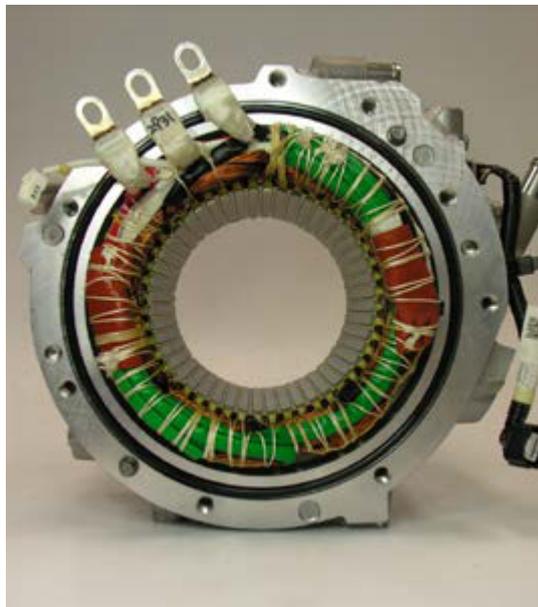
Fig. 1.7: Nissan LEAF stator. Reprinted from [13].

Fig. 1.8: Nissan LEAF rotor. Reprinted from [13].

1.2.4 Advantages and disadvantages

As it was said upper, the PM motors are the most common drives of EV and HEV thanks to their high efficiency and low weight. As stated in [12], [8] and [6], thanks to PM rotor excitation there are no copper losses, so the efficiency increases to 90 % and more. Another positive fact about NdFeB magnets is their high remanent flux density, so less PM material is required. Less PM material leads to the low volume of the whole machine and thus to high power and torque volume density. This machine type also provides high torque at low speed and operates over a wide speed range, so there is no need to add transmission. In [12] is mentioned very good suitability for in-wheel construction. Other advantages, specified in [14], are low noise and torque ripple, almost maintenance-free construction, and easy control. All these benefits caused massive expansion of these machines in electric cars.

The most significant disadvantage of PMSM is the cost of rare-earth magnets and, therefore, the cost of the whole car, which plays a crucial role in today's market. The possibility of irreversible demagnetization due to high temperatures and high stator currents also plays its role. According to [12], the in-wheel construction generates high iron loss at the top of the speed range.

1.3 Switched reluctance machines

As mentioned in the previous section, there is an effort to create PM-less propulsion systems due to the cost of rare-earth materials. One of the possible solutions is switched reluctance motor (SRM), in [12] and [10] called doubly salient reluctance machine, because of salient poles placed not only in rotor but in stator too. The operation principle of this machine type has been known for a long time, but it did not apply to car propulsion due to a lot of noise and torque ripple. Thanks

to the development of control electronics and new control strategies, those negative properties were suppressed. As stated in [12], another way to decrease noise and torque ripple is to use the dual stator system. SRM motor is not widely used, but in [14] it was said that if there were mass production of EV, there would be the simplicity of this machine beneficial in production costs.

1.3.1 Construction and principle of operation

In accordance with [7], SRMs are probably motors with the simplest construction. The basic geometry of the machine is shown in Fig. 1.9. Both the rotor and stator are salient, but the number of pole pairs in the stator is one more than in the rotor. A concentrated excitation winding is located at stator poles, and there is no winding at rotor poles. As mentioned in [15], there are many variations of rotor and stator pole numbers combinations for traction applications like 6/4, 8/6, and 10/12. A higher number of poles reduces the noise, but on the other hand, it increases the number of inverter transistors and, therefore, the frequency of switching, which increases iron loss in stator steel.

The principle of operation is described in [10], [7] and [15]. It is based on the magnetic circuit's tendency to minimize the magnetic reluctance of the whole circuit, and the only way to achieve this is to move the rotor to position under the excited winding pole (for example, A-pole in Fig. 1.9). Opposite stator pole winding is excited by the direct current to create a constant magnetic field of the same direction. As the rotor is close to the position with minimum reluctance, a position sensor instructs power electronics to switch to another phase (for example, B), and the rotor continues to rotate in the clockwise direction. The torque arises thanks to the difference between the d-axis and q-axis synchronous reactance.

1.3.2 Advantages and disadvantages

The main advantage of the SRM motor is its low price, thanks to its simplicity. Production costs are reduced thanks to simply rotor construction without any winding or PM. In [14], and [3], there are discussed advantages like high overload capability, robust construction, maintenance-free operation, wide speed regulation range, flat mechanical characteristics, and better thermal tolerance. According to [6], as there are separate stator phases in case of one phase fault, the machine is able to continue in operation with the remaining phases. Also, high power density and an extended range of constant power are mentioned in [12]. The idea of SRM as the most perspective machine for EV driveline is voiced in [9]. It bases its claim on indisputable advantages of SRM in comparison to IM or PM machines. SMR machine can be slightly more efficient than IM of the same power and using the proper construction
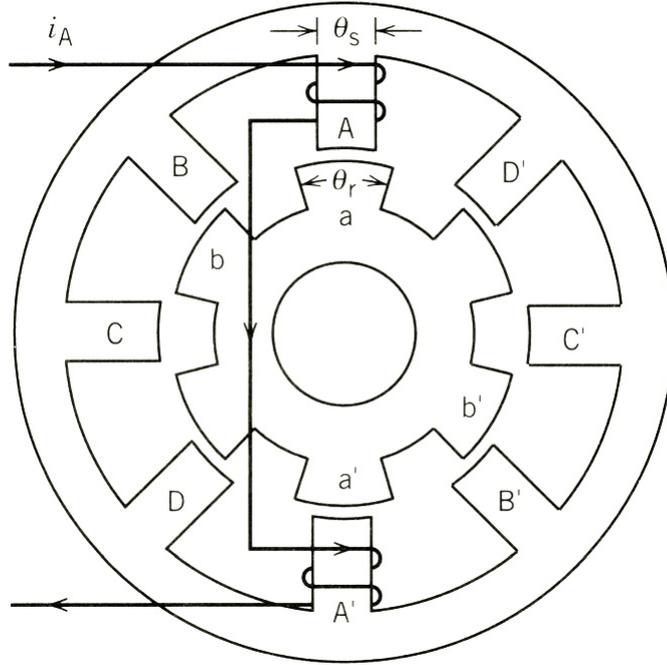
Fig. 1.9: Geometry of switched reluctance motor. Reprinted from [7].

and control strategy, it can match PMSM machines. This statement is confirmed by [15], where the PMSM and SRM of the same parameters were compared. It is possible to achieve the same parameters as PMSM using thin and high-quality iron laminating.

Disadvantages of this machine type were discussed in [12], [9] and [6]. The biggest disadvantage discussed in this literature is a high torque ripple which causes vibrations and acoustic noise. The control system and hardware are also complex because the high non-linearity causes problems with the current-switching angle. The need for IGBT transistors modules and high electromagnetic interference is stated in [14]. These problems cause little use of these machines in EVs. This machine type was installed only in a few vehicles, for example, Land Rover Defender (2013).

1.4 Induction machines

Induction machines are used for various applications, from large industrial propulsion systems to small garden equipment. As cited from [7], an IM is the most common electric machine in the industry. So it is evident that there was an effort to install an asynchronous machine into EV also. Probably the best-known and most successful company in asynchronous machine implementation is Tesla. According to

[16], the Tesla Model S was the most sold electric car in 2015 and 2016. The motor of the Tesla Model S is a good example of a well-designed induction machine for EV propulsion with high efficiency and output power. The main technical data of this motor are summarized in Tab. 1.2.

Tab. 1.2: Tesla Model S motor parameters. Source data from [16].

Parameter	Value	Unit
Power	225	kW
Number of poles	4	-
Maximum speed	15000	rpm
Maximum torque	430	Nm
Stator outer diameter	254	mm
Rotor outer diameter	155,8	mm
Stack length	152	mm

Stator and rotor slot geometry and modeled flux lines in half of the machine are pictured in Fig. 1.10. According to [4], there is three-phase winding in the stator, but in [16] is described the possibility of a six-phase configuration because each phase is made of two parallel paths.
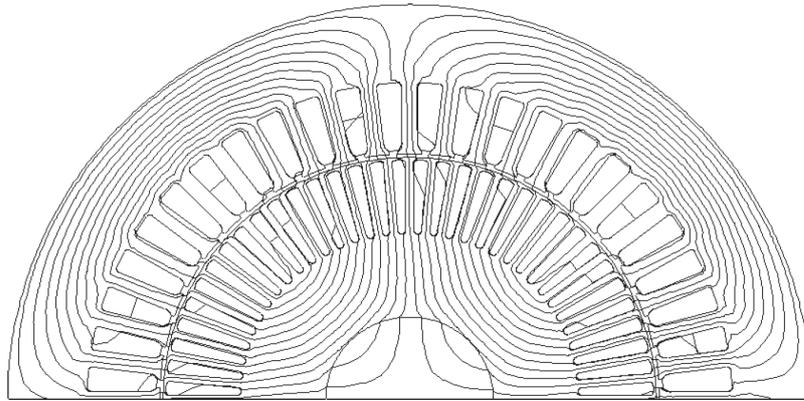
Fig. 1.10: Tesla Model S two rotor poles geometry with flux lines under load. Reprinted from [4].

As shown in Fig. 1.11, the rotor squirrel cage is made of copper. This solution is favorable for decreasing rotor Joule losses because the resistivity of copper is lower than the resistivity of aluminum. In [16] there was made a simulation of the Model S motor considering copper and aluminum as the squirrel cage material. The simulation results showed an increase in efficiency from 91,9 % in the case of aluminum to 93,4 % in the case of copper.

Fig. 1.11: Tesla Model S rotor. Reprinted from [16].

1.4.1 Construction and principle of operation

The stator of the machine is made of laminated steel with slots and stator winding. Stator winding is designed to create sinusoidal air gap magnetic flux. The stator stack with winding is pictured in Fig. 1.12 (a). There are two types of rotor construction, the wound rotor type and the squirrel cage type. Wound rotor winding as three-phase winding with each phase connected to a slip ring is described in [7]. Against slip rings, there are brushes mounted to the stator case. Those brushes can be connected to a three-phase voltage source or resistors. Using resistors enables operating the machine's speed, but it significantly decreases the efficiency. The use of wound-rotor asynchronous machines is a matter of history since the speed can be controlled simply by a frequency converter. In the case of the squirrel cage rotor, the copper-stranded winding is replaced by aluminum or copper solid bars, which are connected by the ring and create a short circuit cage. Because this solution is simpler and maintenance-free, it is used for EV propulsion.

According to [10], the principle of operation is based on the voltage induced into the rotor cage thanks to a slip. At first, the stator's three-phase distributed winding generates a rotating magnetic field inside the stator. As the magnetic field moves, it induces voltage to rotor bars, and thanks to their short circuit connection, the currents are generated. Those currents create a rotor magnetic field, which interacts with the stator magnetic field and moves the rotor. Rotor speed is not similar to the speed of the rotating magnetic field. The difference between them is named slip. The asynchronous machine needs the slip to induce voltage into the rotor winding.

Fig. 1.12: Tesla Model S stator steel pack with winding. Reprinted from [16].

1.4.2 Advantages and disadvantages

Simplicity, low cost, reliability and robustness of IM was stated in [3], [8] and [9]. The technology of this motor type is well known, the manufacturing process is quite simple and well known. As the principle of operation already indicated, it is also PM-free. Production costs are then significantly decreased. Advantages in wide speed range and good regulating properties using field orientation control were discussed in [12]. From the comparison of IM with DC in [8], it follows that the induction machine has higher efficiency than the DC machine.

Due to rotor short-circuited aluminum winding, there are higher losses, decreasing efficiency. The efficiency can be slightly improved by using copper instead of aluminum, as was done in [16]. The required magnetization current, which increases stator copper losses, is pointed out in [8]. All those losses decrease the overload ability and efficiency of the machine. For a lower magnetization current, there is a way of reducing the air gap, but this leads to tighter fabrication tolerances and increases production costs.

1.5 Synchronous brushed machines

The last machine type used for EV propulsion is a synchronous brushed machine. This machine type is used mainly for its PM-free construction.

1.5.1 Construction and principle of operation

The construction of a stator is the same as an asynchronous machine. It is laminated to decrease eddy current losses. In slots, a distributed three-phase winding is placed to create a rotating magnetic field. Excitation of the machine is produced by one DC phase placed at the rotor. An external DC source mostly powers this phase through two brushes and slip rings. According to [7] and [10], there are two variations of rotor geometry. The first one is cylindrical or non-salient pole geometry. As the name implies, the rotor has a long cylindrical shape with a relatively small diameter, so the constant air gap is achieved. The excitation winding is evenly distributed under the rotor surface. These machines are mostly constructed as two-pole machines and used as energy generators powered by a steam turbine.

The second one is a salient pole rotor, and as the name suggests, its construction is based on salient poles with the field winding concentrated around these poles. A model of a salient pole rotor is shown in Fig. 1.13. The number of salient poles is the same as the number of magnetic poles produced by the stator winding. Due to saliency, there is not a constant air gap, so the quadrature and direct inductance are not similar. The salient pole rotor typically has a large diameter and short axial length. It is commonly used as a generator and driven by a water turbine. Sometimes it is necessary to include a damper winding, which is equivalent to the short-circuit cage of the asynchronous machine. This damper winding is designed to start the synchronous motor similarly to asynchronous. After reaching the synchronous speed, the machine is pulled into synchronism with the stator rotating magnetic field. At this moment, the damper winding dampens rotor fluctuation during its operation and helps to keep it in synchronism.
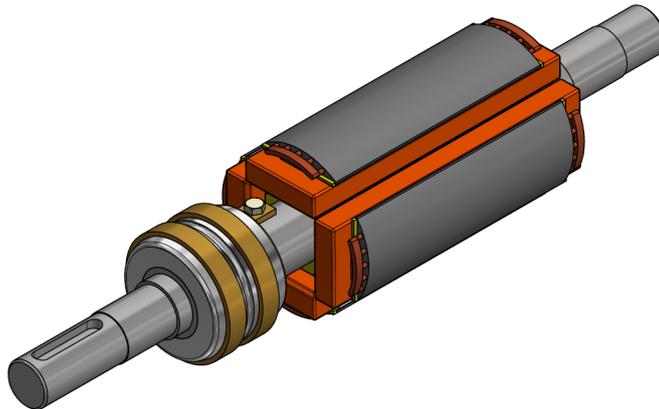
Fig. 1.13: Rotor model of the small salient pole synchronous machine with slip rings.

The working principle of a synchronous machine is based on the similar speed of the stator magnetic field and rotor physical speed. The excitation rotor winding creates a stationary magnetic field that interacts with the rotating magnetic field produced by the stator winding. According to [7], synchronous brushed machines have a helpful feature thanks to the field winding external power supply. It is possible to operate it in overexcited or underexcited mode. During the overexcited mode, the exciting current is higher than necessary, so the machine operates at the leading power factor. If the exciting current is lower than necessary, the machine operates at a lagging power factor and takes a lagging reactive current from the AC supply. This feature gives the possibility to control the power factor of the machine to operate at a unity power factor, and therefore no reactive current is required.

1.5.2 Advantages and disadvantages

The advantage in simpler control than for the PMSM is mentioned in [3]. As stated in [1], due to the increasing cost of rare-earth materials, brushed synchronous machine price is not as higher as it used to be in comparison to other machine types. The improvement in power electronics drives gives SB machines more space on the market. The absence of PM materials in machine manufacturing has also influenced the environmental impact addressed in [17]. The most significant advantage of the SB machine is a variable excitation, which according to [4] and [18], enables the creation of higher starting and low-speed torque compared to PMSM of the same power and stator current, as shown in Fig. 1.14. Another positive fact is that changing the excitation current enables to operate at maximum torque per ampere across the whole speed range and keeps the united power factor, so the power electronics do not have to create additional reactive current. The maximum field current is given when the machine runs at low speed. As the speed increases, the back emf is higher, so the field current is decreased to keep maximum torque per stator ampere. As it was said in [3], the variable field current can be controlled to constant power operation at high speed as shown in Fig. 1.14.

A slip contact using slip rings and brushes could be counted as a disadvantage of this machine type, but according to [3], and [19] the brushes of SBM wear out slower than brushes of DC machine, so their maintenance intervals are long enough to say they are almost maintenance-free. There is a minor disadvantage in peak efficiency, which is slightly lower than the peak efficiency of PMSM. Rotor copper losses cause the efficiency to decrease, but as stated in [19], the efficiency is somewhere between 94 to 96 percent, and this is not so bad. The additional hardware like slip rings, brushes, and DC power supply could slightly increase the price of this machine, but all those technologies are well known, relatively cheap and available, so the cost of
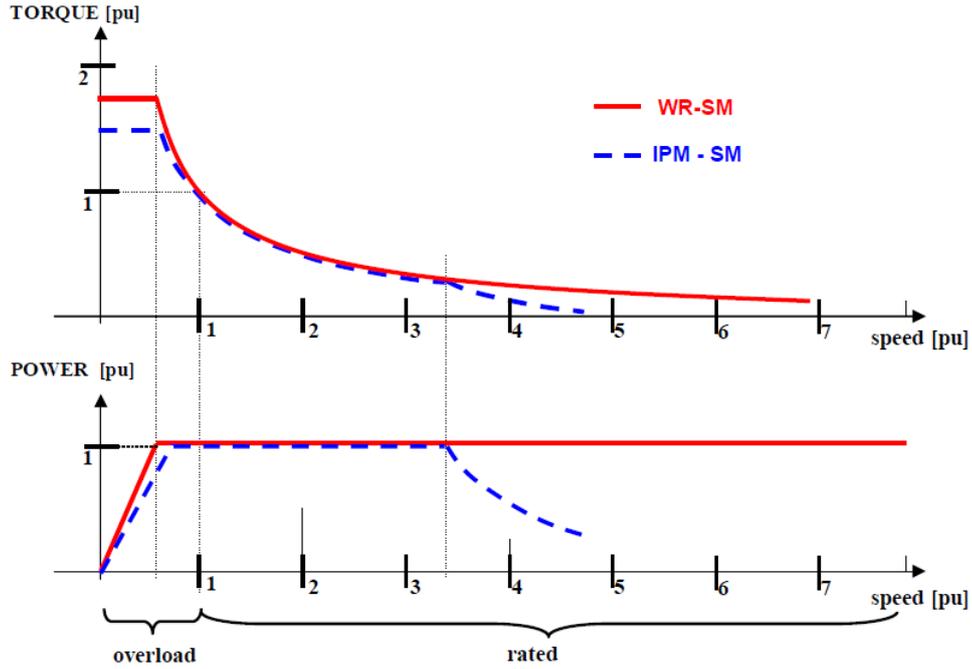
Fig. 1.14: Comparison of wound rotor synchronous machine (WR-SM) and interior permanent magnet synchronous machine (IPM-SM) torque and power characteristics. Reprinted from [18].

the whole car will not be increased at all. The power density is, according to [4], lower in comparison to the PM machine.

1.5.3 Brushed synchronous machine as electric vehicle drive

As mentioned before, the most used electric motor for the EV driveline is the PM machine, but the advantages of the SB machine, rising rare-earth material cost, and the power electronics improvement provide SB machine to take its place on the market. As presented in [19], a Renault is the only car producer who uses SB machines in the serial production of electric cars. Models equipped with this engine are Kangoo, Fluence, and Zoe. The rotor of Renault's R240 motor pictured in Fig. 1.15 is a salient pole machine with slightly modified geometry. The rotor is longer than its diameter, but generally, the opposite is true in the case of a big salient pole machine. This modification is commonly used for low-power machines, mainly operated in a motor mode.

The completed rotor sheets and winded rotor coils around them are shown in Fig. 1.15. Referring to [4], these coils are winded from a small diameter wire with many turns. Due to using a winding automat for the wire placing, are coils connected
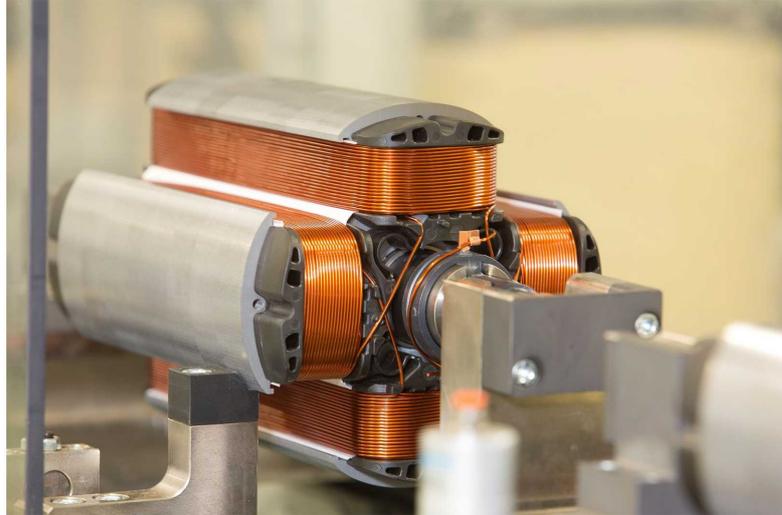
Fig. 1.15: Rotor winding of Renault R240 motor. Reprinted from [20].

in series because the wire is winded without braking. Poles are insulated from each other, and at the end of each pole were placed plastic end tables to stabilize coils during operation. Round aluminum winding holders, placed at the ends of the rotor, are shown in Fig. 1.16. Those holders secure the winding at high speeds and are used for rotor balancing, which is visible in Fig 1.16, where some holes were drilled to balance the rotor.

Fig. 1.16: Complete rotor of Renault R240 motor. Reprinted from [20].

Both ends of the winding are connected to slip rings and brushes, powered from a DC source of the automobile. A detail of slip rings is pictured in Fig. 1.17. The Renault's R240 motor technical specifications are summarized in Tab. 1.3. Due to

the high maximum speed of the machine and high torque requirement, it is necessary to include a reduction gearbox.

Fig. 1.17: Renault R240 rotor slip rings detail. Reprinted from [21].

The electromagnetic simulation of the Renaults R240 motor was performed in [4]. Flux line plot under load is shown in Fig. 1.18. in this figure, the concentration of magnetic flux lines to rotor poles along the direct axis is clearly visible. It is evident that the highest flux density would be achieved at rotor poles, so the pole yoke needs to be wide enough to achieve low flux density but narrow enough to create space for placing the field winding. If it is not possible to make the pole narrow. Then it is necessary to lower the number of turns and use higher current density in the rotor winding. Unfortunately, the higher current density brings an increase in rotor Joule losses. With the increase of rotor Joule losses, the efficiency is getting significantly lower, so a balance of parameters needs to be found.

Tab. 1.3: Renault Zoe R240 motor parameters. Source data from [4].

Parameter	Value	Unit
Power	65	kW
Number of poles	4	-
Maximum speed	11300	rpm
Maximum torque	220	Nm
Number of stator slots	48	-
Number of series turns per phase	40	-
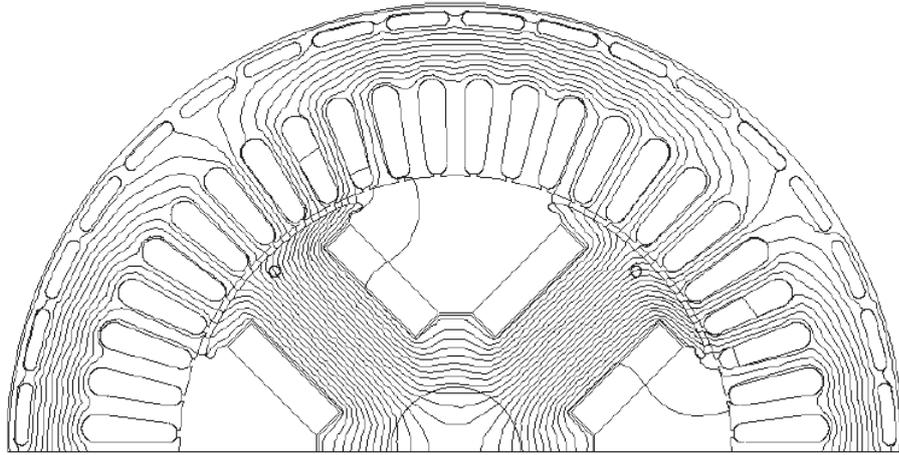
Fig. 1.18: Renault R240 flux plot for two machine poles. Reprinted from [4].

Looking in Fig 1.19, where the air gap flux density is plotted, it is obvious that it is not a pure sine wave. The stator slotting and higher harmonics cause the ripple, and it appears as modulated peaks on the base signal. According to [22], it would be better to use a non-uniform air gap to get a better shape of the air gap flux density.
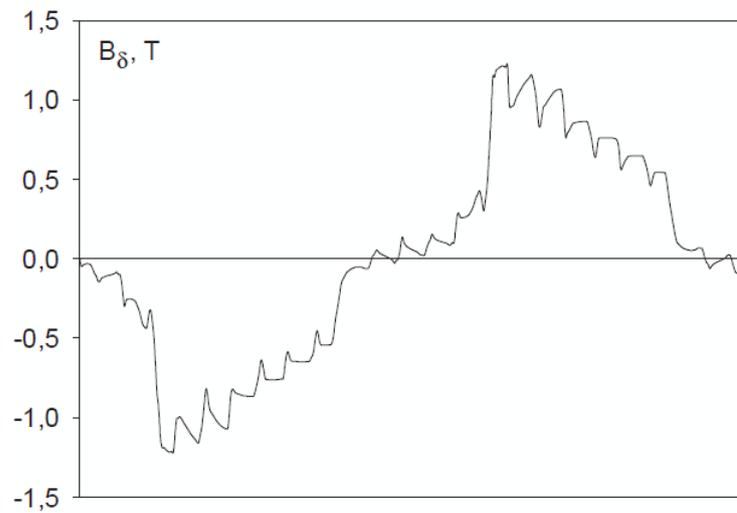
Fig. 1.19: Renault R240 air gap flux density plot. Reprinted from [4].

2 Wound-field synchronous machine for traction applications

At present, machines with rare-earth PM are mainly used for this purpose. However, as pointed out in [1], the price of these magnets is increasing rapidly. That is why, according to [2], there are currently requests searching for a way to avoid the use of rare-earth magnets. One way is to use a wound rotor synchronous machine, as described in [1].

Some modifications need to be made before using a wound-rotor synchronous machine for traction application. Often salient pole synchronous machines are modified for this purpose. As described in [22], SPSM usually has a relatively large rotor diameter in comparison to its length. For traction applications, they are usually longer, and their diameter is reduced, as can be seen clearly in Fig. 1.15. Machines for traction applications are often operated over a wide speed range. By reducing the rotor diameter, the circumferential speed of the rotor is reduced, and therefore the forces acting on the rotor surface are reduced.

Over the past few years, interest in WFSM for traction applications has increased. So, various modifications and improvements to the existing concept of this machine have been proposed. Some of these modifications will be described in the following sections of the thesis.

2.1 Vernier machine

Vernier machines are able to provide high torque density because they work on the principle of the "magnetic gearing effect," which was explained in [23]. The principle is that the number of rotor pole pairs is modulated by the stator teeth, creating a component with the same number of pole pairs as the rotating magnetic field produced by the stator winding. Their interaction creates torque on the machine shaft. One variant of the vernier equation must be satisfied to achieve this effect. Both variants of this equation are typed in equation (2.1).

$$p_{\mathrm{r}} = N_{\mathrm{s}} - p \quad \text{or} \quad N_{\mathrm{s}} + p \tag{2.1}$$

2.1.1 Constuction

The permanent magnet machine was discussed in [23], but the same effect is used for the design of the WFSM in [24]. The advantage of this machine is the possibility of running in two modes. This possibility is given by two rotor field windings,

WS1 and WS2, placed in 20 rotor slots and excited through separate slip rings and brushes. Using different excitation combinations of these two windings makes it possible to change the number of rotor poles. The stator of the machine has three-phase distributed winding in 12 semi-closed slots. The configuration of the machine topology is shown in Fig. 2.1.
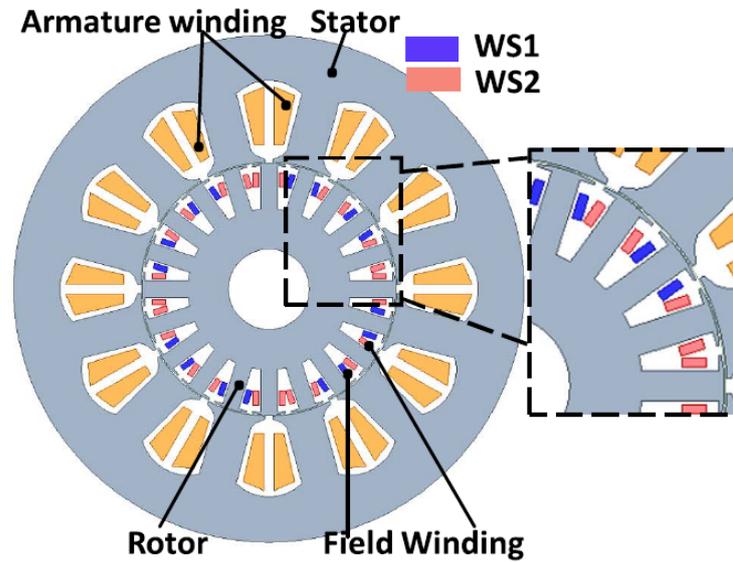
Fig. 2.1: Wound field pole-changing vernier machine topology. Reprinted from [24].

An H-bridge is used to supply and reverse the direct current in the excitation winding. The bipolar part of the bridge is connected to the WS1 winding and the unipolar part to the WS2 winding, as shown in Fig. 2.2. The freewheeling diodes are connected in parallel to the transistors.
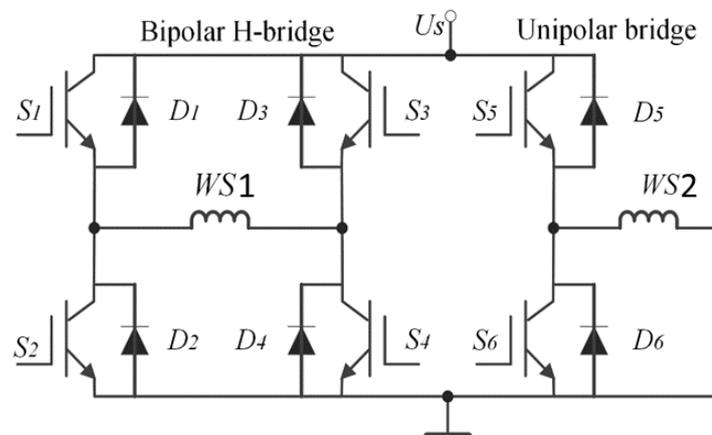
Fig. 2.2: H-bridge for field excitation. Reprinted from [24].

The armature winding is constructed to create a rotating magnetic field with two pole pairs. The number of rotor pole pairs is different for each machine mode. When running in vernier mode, their value is 10, whereas when running in WFSM mode, it is 2. Other important machine parameters are shown in Tab. 2.1.

Tab. 2.1: Proposed machine parameters. Source data from [24].

Parameter	Value	Unit
Terminal voltage in vernier mode	130	V
Terminal voltage in WFSM mode	41,7	V
Stator current	2	A, rms
WS1 and WS2 field DC current	5	A
Number of stator turns per slot	80	-
Number of rotor turns per slot	60	-
Number of stator slots	12	-
Number of rotor slots	20	-

2.1.2 Principle of operation and machine characteristics

The machine starts in the vernier mode, where the current is fed into the rotor windings in such a way that the direction of magnetic flux in each tooth is opposite to that of the adjacent tooth, as shown in Fig. 2.3. By referring to 2.1, this produces a magnetic field that has ten pole pairs that are modulated by the stator teeth. This modulation creates a component with two pole pairs in the air gap flux density. The created component then interacts with the rotating magnetic field of the rotor to create a torque on the shaft. In this mode, the frequency of the inverter is then increased until the rated speed of the machine is reached, as can be seen in Fig. 2.4.
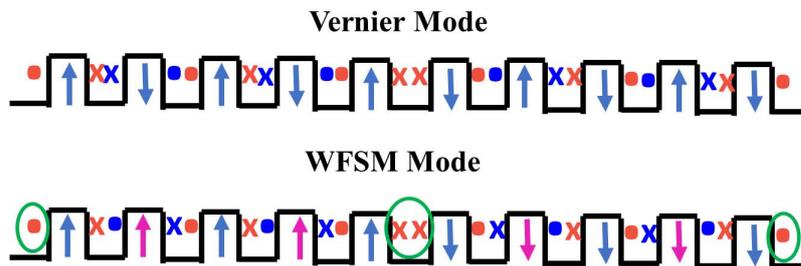
Fig. 2.3: Rotor magnetic flux orientation in both operation modes. Reprinted from [24].

After reaching the rated speed of the machine, the polarity is reversed by changing the current direction in the WS1 winding so that always five adjacent teeth have the same magnetic flux direction as demonstrated in Fig. 2.3. This creates two pole pairs on the rotor, interacting with the stator rotating magnetic field.
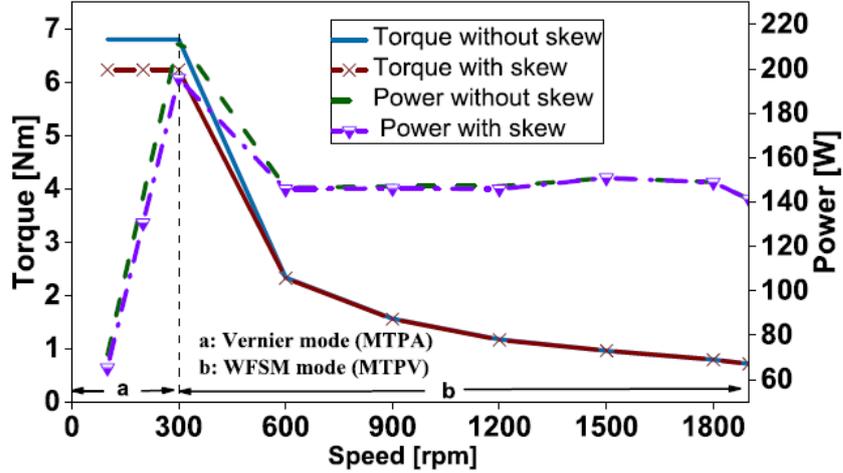
Fig. 2.4: Torque and power speed chracteristics. Reprinted from [24].

In Fig. 2.4, it can be noticed that the output torque of the machine rapidly decreases when going into the WFSM mode and increasing the speed because the machine goes into the constant power region. Thanks to the "magnetic gearing effect," the output torque of the machine is highest in the vernier mode because, in this mode, the back EMF is higher. Further, this figure compares the effect of skew on the machine output and torque for both modes. The value of the skew angle was nine degrees.

Also, the torque ripple is lower than in WFSM mode, where the cogging torque and back EMF creates additional harmonics resulting from five teeth producing magnetic flux in the same direction. When comparing the back EMF in the vernier and WFSM mode in Fig. 2.5, it is noticeable that in the vernier mode, the back EMF has a smoother waveform, so the additional harmonics are lower.

This machine type is suitable for an electric vehicle drive thanks to its possibility to change the number of pole pairs, which gives the machine a wide speed operating range. In vernier mode, it has high torque density, so it is fitting to use it for acceleration and, at higher speeds, switch to WFSM mode. However, as the machine has a high number of rotor pole pairs, it needs to be fed with a high-frequency inverter. Due to high operating frequency, the power factor decreases and core
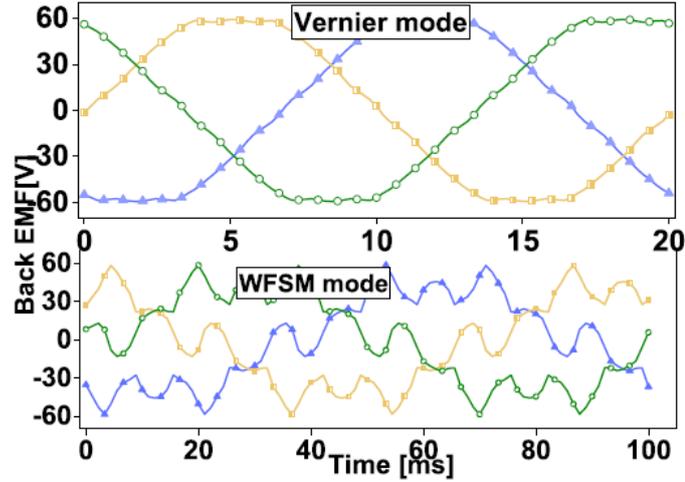
Fig. 2.5: Comparison of back EMF waveforms. Reprinted from [24].

losses increase. The low power factor then increases the required power and price of the source inverter, and high core losses decrease the efficiency of the machine.

2.2 Brushless rotor excitation

The strongest disadvantage of wound-field synchronous machines are brushes and slip rings, so there is a considerable effort to use alternative field winding excitation. The following sections will discuss possible alternatives to the field winding power supply.

2.2.1 Rotary transformer

The first option for contactless energy transfer is to use a rotary transformer, which works on a similar principle to a classic single-phase transformer, the only difference being that one part is static and the other rotary. In most cases, according to [25], the primary winding is located on the static part and is fed by an AC signal. Then, on the rotating part, there is a secondary winding where a voltage is induced. The induced AC signal is then rectified by a rotary rectifier located on the rotor of the operated machine. The cores of both parts are usually made of magnetic material. There is a small air gap between the rotating part and the static part, which can be either axial or radial, as shown in Fig. 2.6. However, as mentioned in [26], the operation of classical rotary transformers is speed-dependent and adds another system dynamic, the time constant. Increasing the weight and length of the machine shaft is also discussed in [27].

(a) Axial air gap.

(b) Radial air gap.
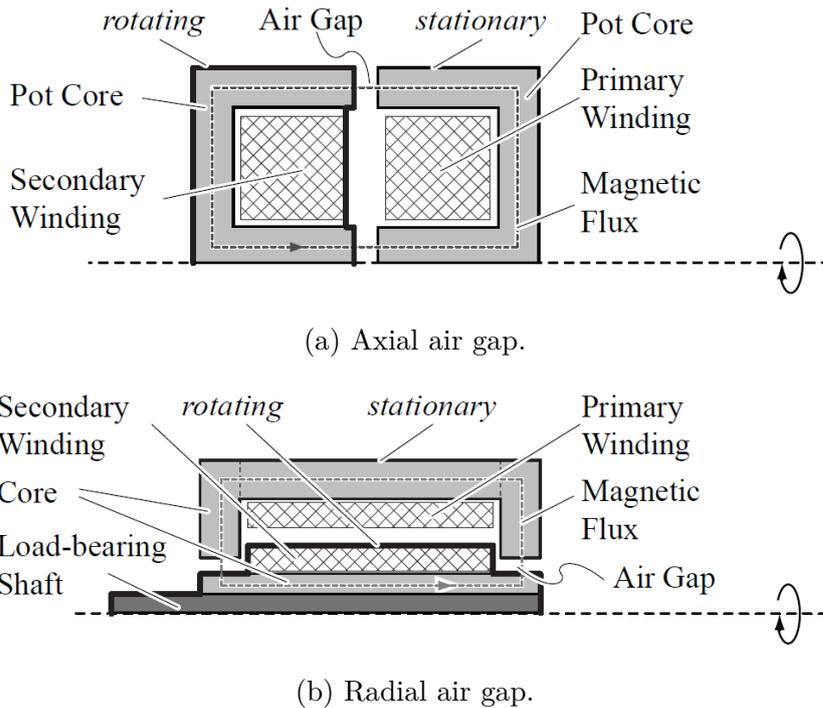
Fig. 2.6: Rotary transformer cross section. Reprinted from [25].

The classical concept of the rotary transformers has a magnetic core, which, by creating a sufficiently small air gap, allows a large magnetic coupling to be achieved. However, on the [25] basis, the presence of magnetic material allows eddy currents and hence losses in the transformer core. Another problem is the mechanical strength of the rotating part at high speeds. Since magnetic steel is a relatively heavy material, large centrifugal forces are generated, limiting the rotation speed. The new concept presented at [28] minimizes these disadvantages by using composite materials instead of magnetic steel on the rotor and interleaved winding that significantly reduces leakage inductances by a factor of four. A topology of the proposed concept is presented in Fig. 2.7.

A model of the rotary transformer based on optimization and interconnection of individual parts of the design was created in [28] using the automated design algorithm. The electromagnetic and mechanical simulations of the designed model found that the maximum transmitted power is 11.3 kW with 97% efficiency. The operating frequency was set at 20 kHz, with the transformer mechanically capable of rotating at speeds up to 20 000 rpm, and since it was designed for 16 000 rpm, a 25% safety margin was achieved. At this speed, the calculated displacement on the outer surface of the rotor was only 0.26 mm, which is not a threat compared to the 2 mm air gap.

The interleaved windings allow for increased magnetic coupling despite the in-
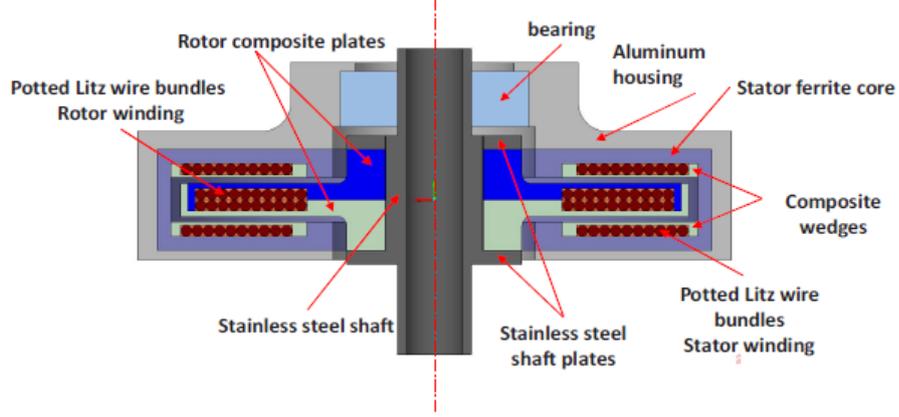
Fig. 2.7: Topology of proposed rotary transformer. Reprinted from [28].

creased air gap, which reduces the requirement for manufacturing accuracy and allows operation at high speeds, commonly achieved in electric vehicle operation. Thanks to resonant capacitor compensation and by applying this topology, it is possible to achieve up to a twofold reduction in volume for the same power transferred, which for the proposed transformer was 10 kW.

2.2.2 Capacitive power transfer

Another option for non-contact power transfer to the rotor winding is a capacitive power transfer. This method, according to [29], involves the use of a rotary capacitor. It works on a similar principle as the tuning capacitor used in old radios, except that its capacitance does not change with rotation angle. It can be designed as an assembly of two concentric hoops or the more commonly used parallel rotating disks.

As mentioned in [27], for combination with WFSM, an axial hydrodynamic configuration was selected. It is an assembly of axially placed stator and rotor aluminum discs. The thickness of each disc is usually around 0.5 mm, and the diameter depends on the required capacity. The size of the air gap must be as small as possible to maximize the capacitance between the plates according to the equation (2.2). The aluminum discs are also coated with a dielectric coating to increase the electrical strength between them, according to [30].

$$C = \frac{\varepsilon A}{g} \tag{2.2}$$

Since the air gap size is tenths of a millimeter, there is a need to ensure the stability of the rotating discs. For this purpose, in [26] are used stator plates with spiral-shaped grooves that create a hydrodynamic thrust bearing between the surfaces of two neighboring discs. The operation medium of this bearing is the ambient

air. The advantage of capacitive transmission, according to [29], is in the reduction of rotating masses compared to the rotating transformer, hence the possibility to operate at high speeds. Furthermore, there is no need to use copper and magnetic steel materials, thus reducing volume. As stated in [30], it is possible to design a CPC that is up to 1/3 the length of a conventional brushless induction exciter, so it can be placed directly behind the rotor iron, minimizing the axial length of the machine. It is, therefore, possible to produce a smaller and potentially cheaper exciter than with the rotating transformer. Also, thanks to non-inductive coupling and correct positioning, there is no need to ensure shielding. The rotor winding current measurement can be implemented on the stator side as it is not temperature-dependent and not affected by saturation. The disadvantage of possible vibration and mechanical stress sensitivity of CPC during the vehicle duty cycle operation was mentioned in [28].

One such CPC has been proposed in [30] and is illustrated in Fig. 2.8. The CPC was designed to transmit a maximum of 2 kW at a frequency range from 500 kHz to 2 MHz. According to [29], the high frequency reduces the impedance of the capacitor, and by using inductors, it is possible to achieve resonance and operate the CPC at a unity power factor. The disc output diameter was set to 100 mm with 0.4064 mm thick of each plate. The hydrodynamic thrust bearing enabled the construction of the air gap with only 0.115 mm length, and this lead to the capacitance of 2.8 nF per plate set.

(a) Exploded model.

(b) Assembly cross-section.
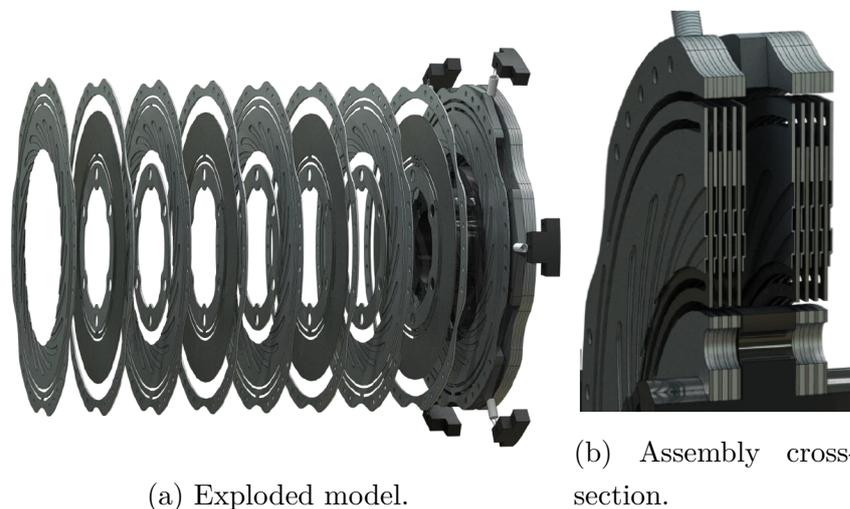
Fig. 2.8: Proposed capacitive power coupler. Reprinted from [30].

2.2.3   Hairpin winding

The last modification of WFSM for the electric vehicle's motor is to use the hairpin winding with square-shaped conductors. With referring to [31], this modification does not have to be used only for wound-field synchronous machines but also for other machines like permanent magnet synchronous or asynchronous machines. Rectangular conductors are mainly used to create the hairpin winding. This type of winding is characterized by the shaping of the coil before insertion into the stator stack, and this, according to [32], simplifies the manufacturing process because the winding faces then have a uniform shape. As mentioned in [33], the winding is then formed by welding the individual coils together to create the required number of turns. The shaping and including of hairpin coils into the stator pack is pictured in Fig. 2.9.
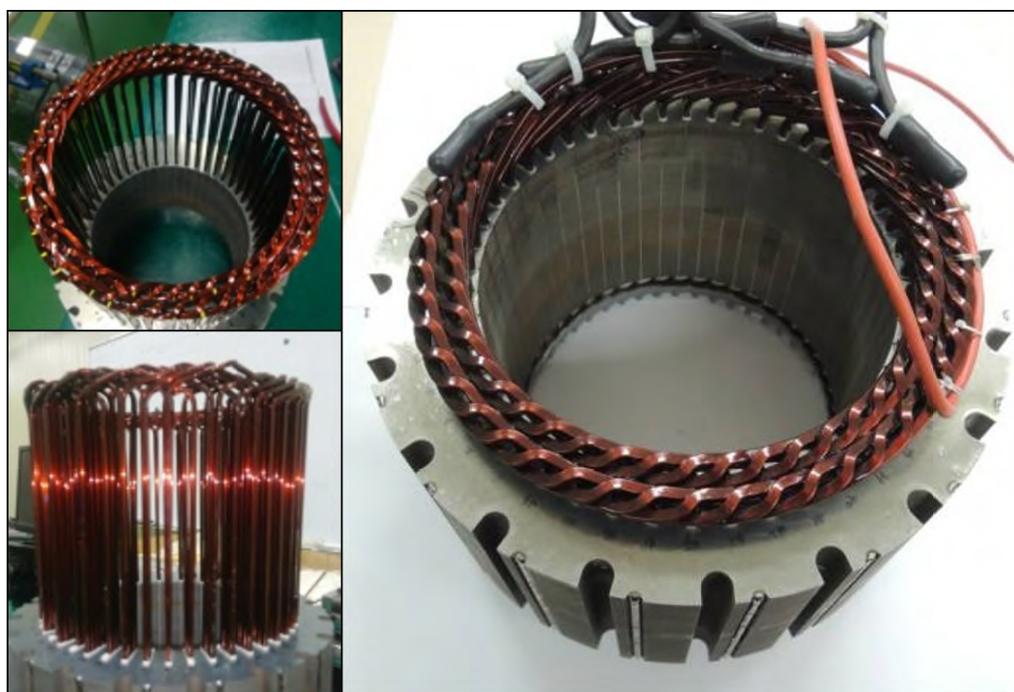
Fig. 2.9: Stator of an improved WFSM. Reprinted from [32].

As shown in Fig. 2.10, the use of rectangular-shaped conductors and stator slots allows a significant increase in the space factor of the winding so that the dead space created by using circular conductors is highly reduced. As noted in [31], this allows the stator tooth width to be increased. Wider stator teeth have a positive effect on reducing iron losses and vibrations that generate noise, which is also desirable in the electric automobile.

By increasing the space factor, it is possible to increase the cross-sectional area of the used conductors. In [32] this led to a reduction in stator copper losses, which
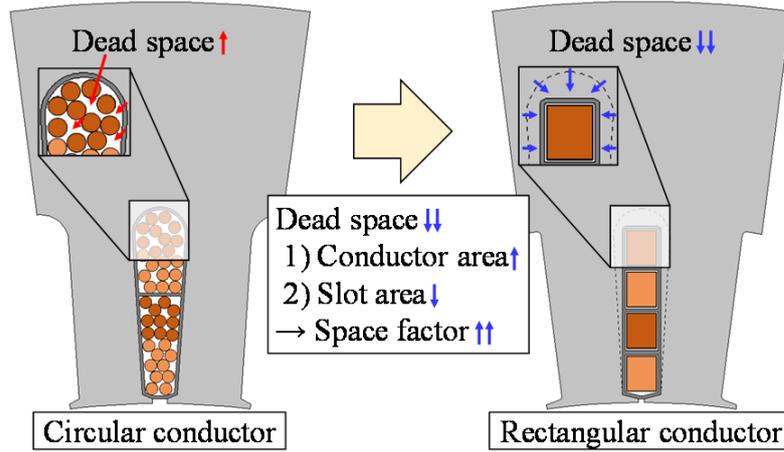
Fig. 2.10: Transition from circular to rectangular conductors. Reprinted from [33].

in [33] are considered to be the majority in the duty cycle of the electric car. The reduction in losses then leads to an increase in the motor efficiency while keeping output power.

If rectangular conductors are used, the skin effect must be considered when operating the machine at high speed. Therefore, the equation (2.3) from [32] is used to determine the skin depth. Based on the calculated skin depth, a rectangular conductor of such dimensions is then selected so that the radius of the circle drawn around the conductor is smaller than the calculated skin depth.

$$\delta = \sqrt{\frac{1}{\pi f \mu_0 \mu_\mathrm{r} \sigma}} \tag{2.3}$$

Since all coils have the same shape, the (2.4) equation can be used to determine the resistance of the individual stator phases at a given operating temperature quite accurately, and that allows the calculation of winding losses in machine design.

$$R_\mathrm{s} = \rho_\mathrm{C} \cdot \frac{2 \cdot (L_\mathrm{stk} + \pi(\tau_\mathrm{s}/2)) \cdot N_\mathrm{ph}}{A_\mathrm{cond}} \cdot [1 + \alpha \cdot (T - 20)] \tag{2.4}$$

As mentioned in [32], the skin effect can also appear in the excitation winding. Due to the armature reaction, currents are induced into the DC winding of the rotors, which fluctuate, and as the high operating frequency is used, the skin effect occurs. Therefore, it is necessary to determine the current ripple and calculate the penetration depth according to the (2.3) equation. The conductor diameter must then be smaller than the calculated skin depth. The resistance of the excitation winding is then calculated using equation (2.5), which also considers winding coil ends.

$$R_\text{f} = \rho_\text{C} \cdot \frac{2 \cdot (L_\text{stk} + \tau_\text{f} + 2h_\text{ec}) \cdot N_\text{f}}{\pi \cdot r_\text{f}^2} \cdot [1 + \alpha \cdot (T - 20)] \qquad (2.5)$$

These equations were used in [32] to calculate the resistance and subsequently the losses in the design of the improved WFSM. The original WFSM was fabricated using the conventional stator coil winding method with round wire. Subsequently, an improved motor was designed and achieved a 0.7% higher energy efficiency while keeping the output parameters, with an 8.5% reduction in motor volume. The power density was increased from 2.12 kW/kg to 2.30 kW/kg. This improvement in machine parameters was achieved by applying stator hairpin winding with rectangular conductors, illustrated in Fig. 2.9. Furthermore, the rotor winding was modified based on the above equations to avoid the skin effect.

3 WFSM modeling

To analyze a wound-rotor synchronous machine, it is necessary to create a mathematical model. For this purpose, equivalent circuits and equations derived from them are used. With the help of these equivalent circuits and equations, it is possible to simulate the output parameters of the machine and analyze them.

3.1 Equivalent circuits

It is possible to make the equivalent circuits of WFSM and equations in different reference frames. In [34], they are represented in a rotor reference frame that spins at the same electrical speed as the rotor. This makes the stator magnetizing inductances constant, so there is no need to model the inductances as a function of rotor position. The resulting equations are then simpler.

Based on [35], equivalent circuits for synchronous machines are created separately in the d- and q-axis. Due to its construction, the salient pole machine is already magnetically anisotropic since the windings are concentrated around the rotor poles. The nonsalient pole construction is isotropic, but according to [34] contains enough anisotropy to be represented by the d- and q-axis model pictured in Fig. 3.1 and Fig. 3.2.
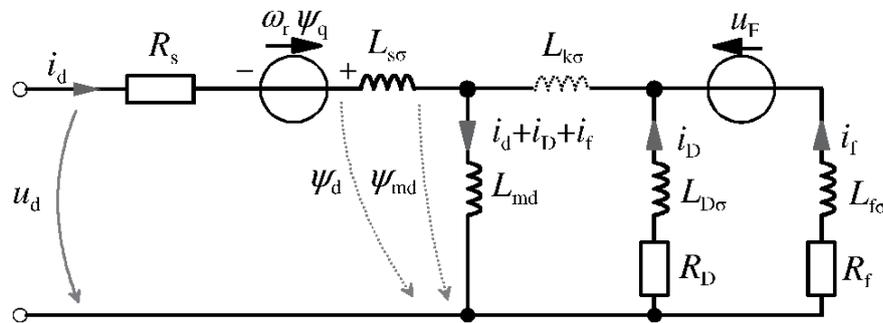
Fig. 3.1: Synchronous machine equivalent circuit in the d-axis. Reprinted from [34].

The representation of these equivalent circuits in the rotor reference frame results in DC circuits. If the machine is in a steady state, then the values of variables such as voltages, currents, and flux linkages are constant. During transients, AC components are created in these variables, especially those representing the damper winding. During the steady state, the variables related to the damper winding are zero.
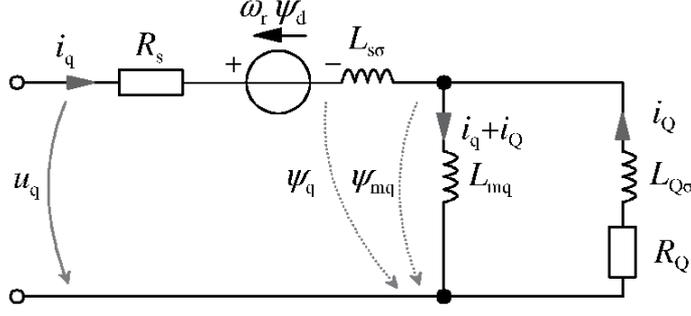
Fig. 3.2: Synchronous machine equivalent circuit in the q-axis. Reprinted from [34].

3.2 Mathematical description of the machine

As mentioned in [34], due to the design of the synchronous machine, the excitation winding is positioned to magnetize the machine in the d-axis direction. To model the parameters of a synchronous machine, it is possible to start from the basic stator voltage equation in the rotor reference frame.

$$\hat{u}_s = R_s \hat{i}_s + \frac{d\hat{\psi}_s}{dt} + j\frac{d\phi_r}{dt}\hat{\psi}_s \tag{3.1}$$

The first part of the equation represents the voltage drop across the stator winding resistance. The second part is the induced voltage generated by the change in the flux linkage. The last part represents the voltage generated by rotation. Since the equation is written in a rotor reference frame, it is induced by fictitious rotating stator winding. As the equation (3.1) is in vector form, based on the equivalent circuits in Fig. 3.1 and 3.2 will be rewritten into the d- and q-axis components. The same equations were used to model the synchronous machine in [36].

$$u_d = R_s i_d + \frac{d\psi_d}{dt} - \omega_r \psi_q \tag{3.2}$$

$$u_q = R_s i_q + \frac{d\psi_q}{dt} + \omega_r \psi_d \tag{3.3}$$

Since it is a wound rotor synchronous machine, its excitation is provided by the rotor winding. The voltage equation (3.4) represents the excitation circuit of the machine.

$$u_f = R_f i_f + \frac{d\psi_f}{dt} \tag{3.4}$$

Two more voltage equations are added if the rotor damper winding is also considered. As the damper winding is short-circuited, the equation consists only of the

right-hand side, where the voltage drops on the resistors and the induced voltage are calculated.

$$0 = R_{\mathrm{D}}i_{\mathrm{D}} + \frac{\mathrm{d}\psi_{\mathrm{D}}}{\mathrm{d}t} \tag{3.5}$$

$$0 = R_{\mathrm{Q}}i_{\mathrm{Q}} + \frac{\mathrm{d}\psi_{\mathrm{Q}}}{\mathrm{d}t} \tag{3.6}$$

The model inductances of the machine need to be defined to establish the flux linkages. The following equations define those model inductances.

$$L_{\mathrm{d}} = L_{\mathrm{md}} + L_{\mathrm{s}\sigma} \tag{3.7}$$

$$L_{\mathrm{q}} = L_{\mathrm{mq}} + L_{\mathrm{s}\sigma} \tag{3.8}$$

$$L_{\mathrm{f}} = L_{\mathrm{md}} + L_{\mathrm{f}\sigma} + L_{\mathrm{k}\sigma} \tag{3.9}$$

$$L_{\mathrm{D}} = L_{\mathrm{md}} + L_{\mathrm{k}\sigma} + L_{\mathrm{D}\sigma} \tag{3.10}$$

$$L_{\mathrm{Q}} = L_{\mathrm{mq}} + L_{\mathrm{Q}\sigma} \tag{3.11}$$

As mentioned in [34], a Cannay inductance parameter $L_{\mathrm{k}\sigma}$ was added to increase the correctness of the real machine representation. It considers the difference in the magnetic coupling of the excitation and damper winding from the magnetizing inductance in the d-axis. The calculations of flux linkages in different components can be written using the following equations.

$$\psi_{\mathrm{d}} = L_{\mathrm{d}}i_{\mathrm{d}} + L_{\mathrm{df}}i_{\mathrm{f}} + L_{\mathrm{dD}}i_{\mathrm{D}} \tag{3.12}$$

$$\psi_{\mathrm{q}} = L_{\mathrm{q}}i_{\mathrm{q}} + L_{\mathrm{qQ}}i_{\mathrm{Q}} \tag{3.13}$$

$$\psi_{\mathrm{f}} = L_{\mathrm{df}}i_{\mathrm{d}} + L_{\mathrm{f}}i_{\mathrm{f}} + L_{\mathrm{dD}}i_{\mathrm{D}} \tag{3.14}$$

$$\psi_{\mathrm{D}} = L_{\mathrm{dD}}i_{\mathrm{d}} + L_{\mathrm{fD}}i_{\mathrm{f}} + L_{\mathrm{D}}i_{\mathrm{D}} \tag{3.15}$$

$$\psi_{\mathrm{Q}} = L_{\mathrm{dQ}}i_{\mathrm{q}} + L_{\mathrm{Q}}i_{\mathrm{Q}} \tag{3.16}$$

With the simplification where inductances L_{dD} and L_{df} are equal to the magnetizing inductance in the d-axis and similarly the inductance L_{dQ} to the inductance in the q-axis, equations from (3.12) to (3.16) can be simplified as follows.

$$\psi_d = L_{md}(i_d + i_f + i_D) + L_{s\sigma}i_d \tag{3.17}$$

$$\psi_q = L_{mq}(i_q + i_Q) + L_{s\sigma}i_q \tag{3.18}$$

$$\psi_f = L_{md}(i_d + i_f + i_D) + L_{f\sigma}i_f + L_{k\sigma}i_D \tag{3.19}$$

$$\psi_D = L_{md}(i_d + i_f + i_D) + L_{k\sigma}i_f + L_{D\sigma}i_D \tag{3.20}$$

$$\psi_Q = L_{mq}(i_q + i_Q) + L_{Q\sigma}i_Q \tag{3.21}$$

The electromagnetic flux equation in the rotor reference frame from [37] is used to determine the torque of the synchronous machine.

$$T_e = \frac{3}{2}p(\psi_q i_q - \psi_d i_d) \tag{3.22}$$

Using the equations for the calculation of flux linkages and various adjustments, an equation for the calculation of the machine moment was obtained, where according to [34] the component $(L_d - L_q)i_d i_q$ represents the reluctance flux, which is generated only in the salient-pole machine due to magnetic asymmetry. The second torque component is generated by the excitation current and the current in the q-axis, so it is the main torque component of the machine. The damper winding generates the last two components and is only considered during transients.

$$T_e = \frac{3}{2}p[(L_d - L_q)i_d i_q + L_{md}i_f i_q + L_{md}i_D i_q - L_{mq}i_Q i_d] \tag{3.23}$$

3.3   Vector diagram

The relationships between mentioned variables can also be described using a phase diagram. Since, for the use in an electric vehicle, the primary consideration is the operation of the synchronous machine in motor mode, Fig. 3.3 shows the vector diagram of a synchronous machine in motor mode. The diagram is shown at a steady state, so the damper winding variables are not included. As mentioned in [34], the vector diagram represents the machine with the rotor spinning in a counterclockwise direction, and as this diagram is in the rotor reference frame, it rotates in the same direction.

Fig. 3.3: The vector diagram of synchronous machine in motor mode. Reprinted from [34].

As stated in [10], the stator flux linkage can be calculated from the voltage $\hat{u}'_s$, which is the stator voltage $\hat{u}_s$ without the voltage drop in the stator winding resistance. Since the machine is in motor mode, the stator flux linkage vector is lagged 90° behind the stator voltage vector. The air gap flux linkage $\hat{\psi}_m$ is calculated from the stator flux linkage by subtracting the leakage flux linkage $\hat{\psi}_{s\sigma}$. The flux linkage generated by the excitation winding is transformed into a direct and quadrature axis via the armature reactions.

The stator flux linkage induces a back emf $\hat{e}_s$, which is almost opposite to the voltage of the power supply. If this voltage is added to the voltage of the power supply, the machine current can be calculated using the equation (3.24).

$$\hat{i}_s = \frac{\hat{u}_s + \hat{e}_s}{R_s} \tag{3.24}$$

As mentioned in [34], the stator flux linkage induces the back emf $\hat{e}_s$, the air gap flux linkage induces a back emf $\hat{e}_m$. This voltage is important when the machine loses currents in the stator winding. When the stator flux linkage results from the field weakening lower than the air gap flux linkage, the terminal voltage increases very fast. It is a dangerous situation because the voltage can reach the maximum value, which is limited only by the used magnetic core material.

4 Machine analysis script

The main goal of this thesis was to create a script for wound-field synchronous machine analysis. The ANSYS Maxwell program was chosen for the finite element method (FEM) analysis of the machine, and a Python programming language was used to write the script.

4.1 Data transformation

The main task of the created script is to analyze the wound-rotor synchronous machine operating characteristics. Since this script was not intended to set up the FEM analysis itself, a model of a small salient pole synchronous machine was used as a data source to set up the transformation from a three-phase system to a rotor reference frame. Because the machine had already been designed and calculated, the calculated data were used as source data for the transformation. The torque characteristic of the wound-field synchronous machine in motor mode was used to verify the transformation of currents and flux linkages. In this case, it was a simulation where the motor runs at a constant speed and then is loaded, so it is a graphical dependence of the torque on time. The characteristic was then obtained using the equation (3.22). The inputs of this equation are the stator currents and flux linkages in the rotor reference frame. These input values were obtained using transformation from the phase values to the d- and q-axes based on the following equations from [34].

$$i_\mathrm{d} = \frac{2}{3}[i_\mathrm{sU}\cos\theta_\mathrm{r} + i_\mathrm{sV}\cos(\theta_\mathrm{r} - \frac{2}{3}\pi) + i_\mathrm{sW}\cos(\theta_\mathrm{r} - \frac{4}{3}\pi)] \tag{4.1}$$

$$i_\mathrm{q} = -\frac{2}{3}[i_\mathrm{sU}\sin\theta_\mathrm{r} + i_\mathrm{sV}\sin(\theta_\mathrm{r} - \frac{2}{3}\pi) + i_\mathrm{sW}\sin(\theta_\mathrm{r} - \frac{4}{3}\pi)] \tag{4.2}$$

The calculated values of the stator currents and flux linkages from FEM simulation in ANSYS Maxwell were loaded within the Python script and stored as vectors. A transformation matrix C was created to calculate the required inputs in the rotor reference frame, then transposed and used for multiplication with the vector of currents and flux linkages according to the equations (4.4) and (4.5).

$$C = \frac{2}{3}\begin{bmatrix} \cos\theta_\mathrm{r} & -\sin\theta_\mathrm{r} \\ \cos(\theta_\mathrm{r} - \frac{2}{3}\pi) & -\sin(\theta_\mathrm{r} - \frac{2}{3}\pi) \\ \cos(\theta_\mathrm{r} - \frac{4}{3}\pi) & -\sin(\theta_\mathrm{r} - \frac{4}{3}\pi) \end{bmatrix} \tag{4.3}$$

$$\begin{bmatrix} i_{\mathrm{d}} \\ i_{\mathrm{q}} \end{bmatrix} = C^{\mathrm{T}} \begin{bmatrix} i_{\mathrm{sU}} \\ i_{\mathrm{sV}} \\ i_{\mathrm{sW}} \end{bmatrix} \tag{4.4}$$

$$\begin{bmatrix} \psi_{\mathrm{d}} \\ \psi_{\mathrm{q}} \end{bmatrix} = C^{\mathrm{T}} \begin{bmatrix} \psi_{\mathrm{sU}} \\ \psi_{\mathrm{sV}} \\ \psi_{\mathrm{sW}} \end{bmatrix} \tag{4.5}$$

After the transformation of input variables to the rotor reference frame, the vector of torque was calculated using equation (3.22). This vector was then graphically interpreted with dependence on the simulation time. The simulation time was chosen as 150 ms and the simulation time step was 0.2 ms. The same characteristic in ANSYS Maxwell was simulated to verify the transformation and torque calculation. Both characteristics were plotted into the same graph, which is plotted in Fig. 4.1. In this graph, the T calculated is the torque calculated in Python script, and the T simulated is taken from FEM analysis in ANSYS Maxwell.
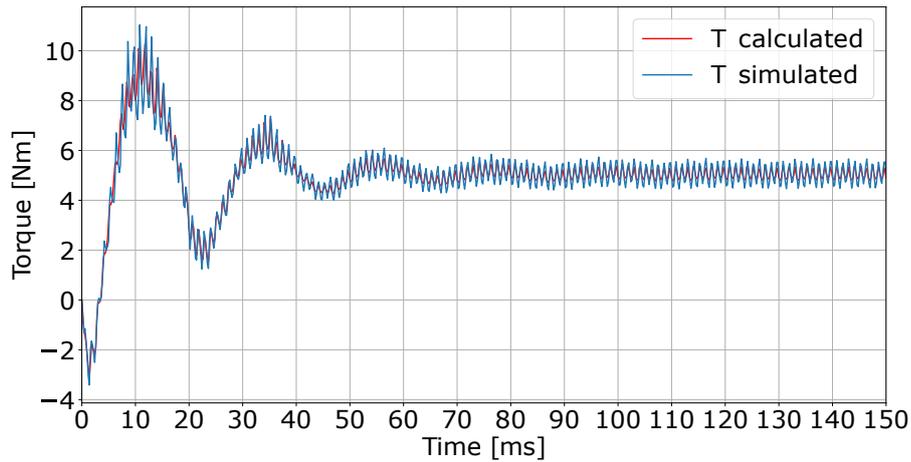
Fig. 4.1: Synchronous machine torque plot. T calculated is the torque calculated using Python script and T simulated is the torque simulated in ANSYS Maxwell.

It is visible that the two waveforms are very similar and overlap each other. This result indicates a correctly realized transformation of the data taken from the simulation results. The average values of both torques were also calculated within the script. Due to transients at the beginning of the simulation, these values were calculated from the last two current periods of the simulation. The average torque calculated in the Python script was 5.053 Nm, and the average torque from ANSYS Maxwell was 5.047 Nm. The RMS values of phase currents were also calculated in

Python, their average value was 11.62 A, and the average value of those currents in the simulation was 11.64 A. The calculated and simulated values were very similar, which is a reasonable verification of the correctness of the calculation.

4.2 Simulated data

Analysis of the machine is made from the initial data generated by the FEM simulation. The source data for this analysis were obtained from the Institute of Electric Drives and Power Electronics at Johannes Kepler University in Linz. At first, the training data for script building were generated. The imaginary wound field machine was designed and simulated using FEM simulation to build the script as universally as possible. Various combinations of input current were simulated to estimate the output torque in specified load points. Those current combinations are plotted to 3D space in Fig. 4.2. These data were not simulated as a function of time but only as a function of the rotation angle. Hence, they are speed independent, and it is possible to analyze the machine at different speeds.
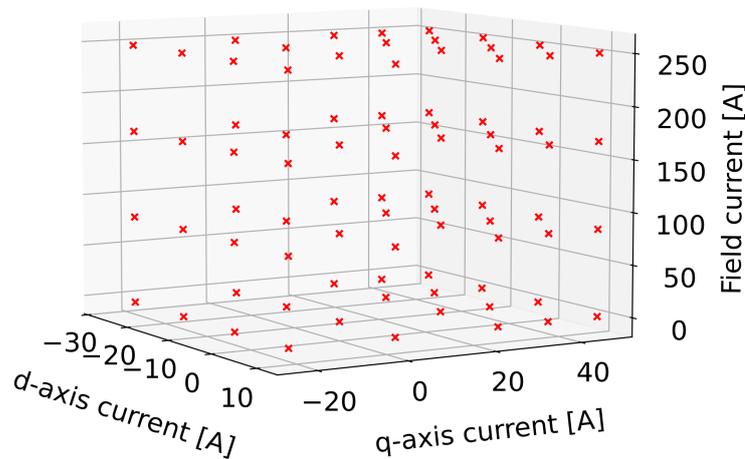
Fig. 4.2: Graphical representation of the training data currents in the 3D space.

As seen in Fig. 4.2, for each of the four field current values were combined four values of d-axis current with five values of q-axis current. The first field current one is 0 A, so for this value, the torque characteristics comparison in Fig. 4.3 was not made because the obtained torque was very low. As the wound rotor synchronous machine needs the flux generated by the field current to produce torque, it should be theoretically equal to zero, but some low torque could be generated by the magnetic remanence phenomena explained in [38]. Since, in this case, a simulated data pack

was used, it is more likely to be a numerical error in the simulation method. Values of current combinations were summarised in Tab. 4.1. As can be seen from Fig. 4.2, some of these values were negative, but their numerical values were the same.

Tab. 4.1: Training data current combination values.

Parameter	Values			
Field current [A]	0	83.3	166.6	249.9
d-axis current [A]	0	11.8	23.6	-
q-axis current [A]	0	23.6	35.3	47.1

A system of per-unit values was chosen to improve the clarity of graphs and figures. Also, the RBF worked better with per-unit values in this case. The highest value of each current in Tab. 4.1 was then used as a reference value for per-unit system determination. As the reference value of the torque, the highest value of 0.58 Nm was set.

The per-unit system was then used in Fig. 4.3 where the RBF used for 3D approximation was tested. According to [39], it is possible to use the RBF for multidimensional interpolation. In [40], the RBF is used for the approximation in 2D, which means that there are two independent variables on the x and y axes and one dependent variable, which is then approximated to axis z. Nevertheless, the wound-rotor synchronous machine is controlled by three different currents. On the stator side, it is the d-axis and q-axis current. Those currents are determined by the combination of the three-phase input currents fed from the network or mostly from the inverter. The field current is fed into the rotor winding through slip rings. So there are then three independent variables and one dependent, which means the approximation in 3D space. That was the reason why the comparison of 2D and 3D RBF approximation was made in Fig. 4.3. The approximation of torque versus current in the d and q axis was performed manually for rotor winding currents of 83.3, 166.6, and 249.9 A. Subsequently, the torque versus d-axis, q-axis, and field currents was approximated. From this approximation were then selected graphs that correspond with defined field current values. As can be seen from Fig. 4.3, the plots of generated graphs are very similar, with only minor variations in the maximum values. From this, it can be concluded that RBF interpolation works for three independent variables and can therefore be used further.

4.2.1 Torque characteristics

When using the RBF function to approximate the torque versus input currents combination, the results can be displayed at most in a 3D spatial graph, and more
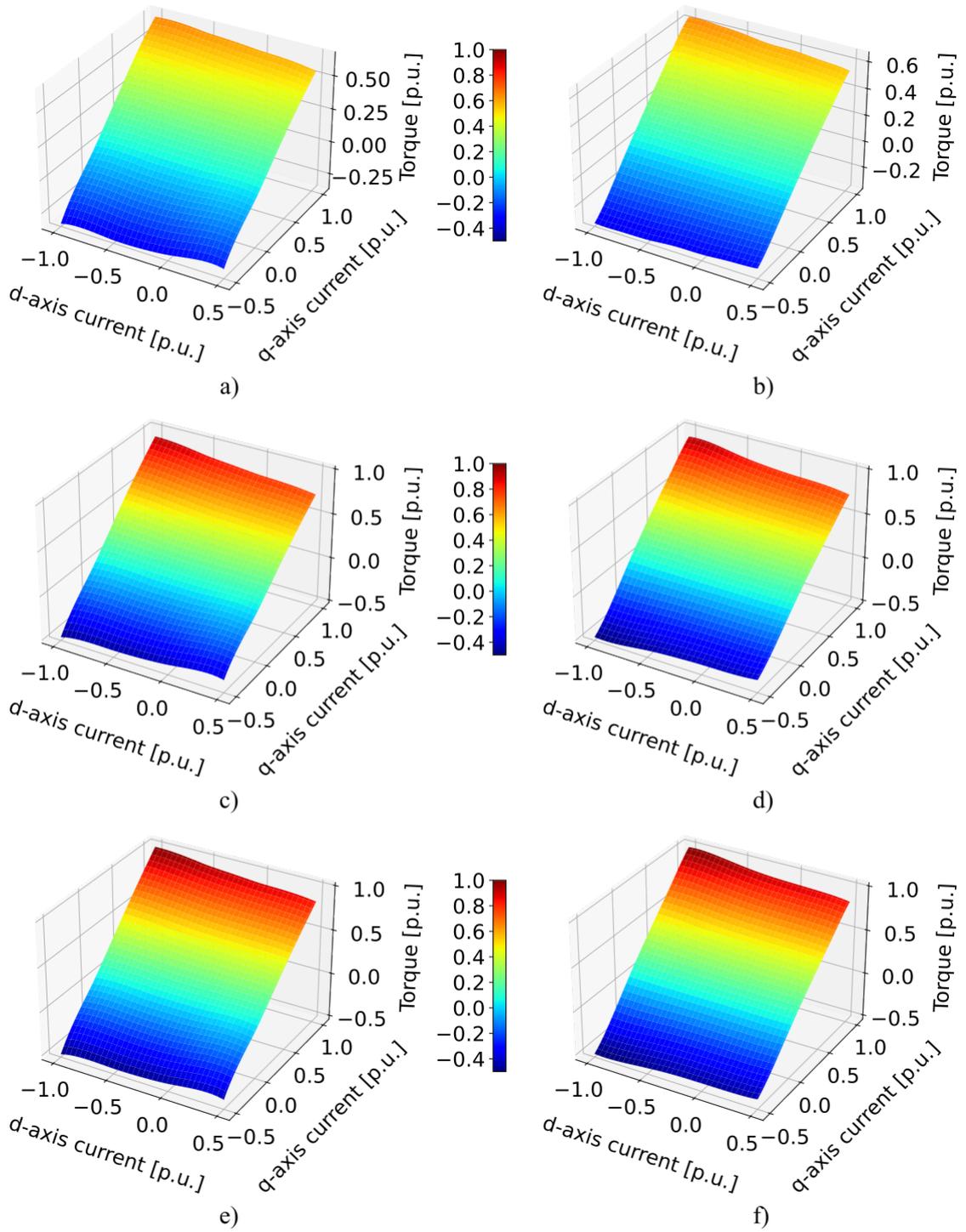
Fig. 4.3: Comparison of torque characteristics obtained from 2D (a, c, e) and 3D (b, d, f) interpolation for rotor field current 83.3 A (a,b), 166.6 A (c,d) and 249.9 A (e,f).

of these graphs need to be created. To show the dependence on all variables, since it is always possible to show the dependence of the torque on only two of the three variables. Therefore, all three possible combinations of these graphs are depicted in Fig. 4.4. As it is not possible to display the fourth dimension, torque characteristics were displayed for the value of the fourth dimension, where the highest torque is achieved.
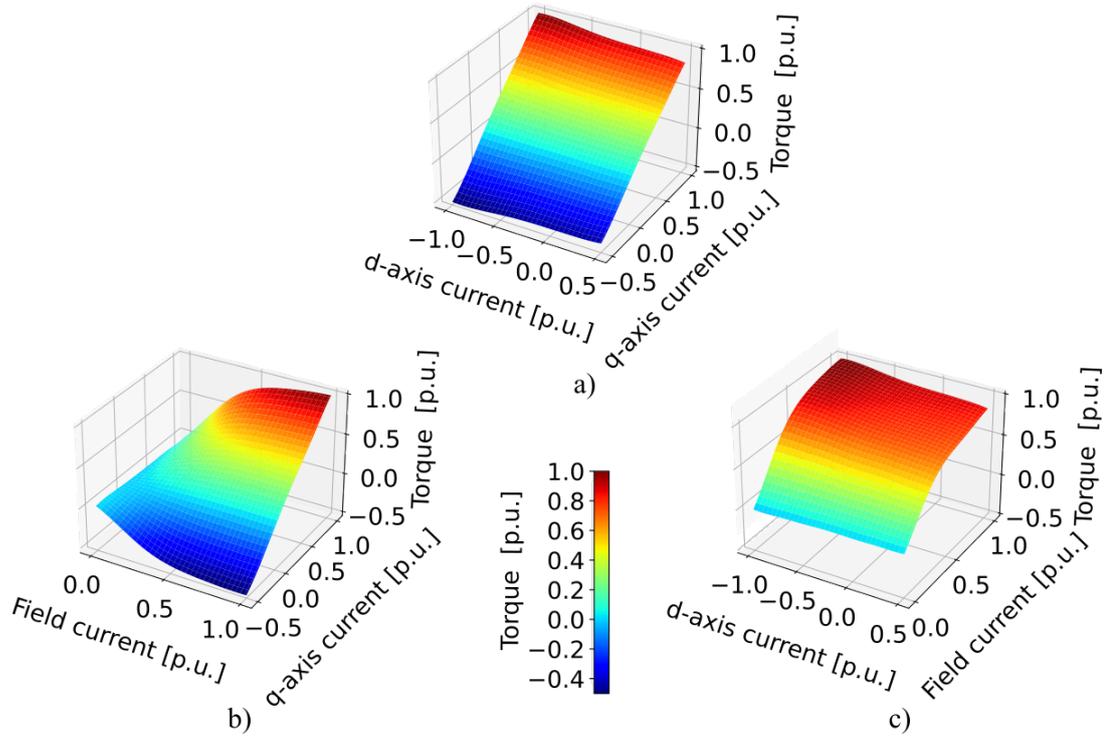
Fig. 4.4: Graphical dependence of the training torque values on a) d- and q-axis, b) Field and q-axis, c) Field and d-axis current.

In the plots of torque versus excitation current and currents in the d- or q-axis, it is possible to notice a relatively rapid increase in torque around 0.5 p.u. of excitation current. Although the torque increases with increasing excitation current, this increase is not as significant. It can also be assumed that as the excitation current increases, the losses in the rotor will also increase, and since the torque does not increase as fast as the losses, the efficiency will decrease.

4.2.2 Electromagnetic efficiency calculation

Another part of the script was built to calculate the electromagnetic efficiency of the machine at individual load points. Since the source data does not contain information about the machine terminal voltage or machine mechanical and additional

losses, the efficiency is calculated only from the machine joule and core losses and the power at the shaft. As there are not included mechanical and additive losses, the obtained results are values of electromagnetic efficiency. Thus, if the machine efficiency is discussed in the following part of the thesis, the electromagnetic efficiency is mentioned. Therefore, the following section describes the methodology for calculating machine losses and the subsequent determination of the efficiency.

Joule losses significantly affect machine efficiency, especially in the case of wound-field synchronous machines. The resistance of stator and rotor winding was included in simulated data provided by JKU, so the Joule losses in every single stator phase and rotor winding were, according to [7], calculated using equation (4.6).

$$\Delta P = R_{\text{s/r}} \cdot I_{\text{s/r}}^2 \tag{4.6}$$

As the stator Joule losses are calculated separately for each phase, it is possible to sum them to one variable ΔP_{sCu}. It is unnecessary to calculate the value of losses in the rotor for individual poles separately since the value of the total resistance of the excitation winding is given in the source data, so the winding faces and transitions between separated poles are included.

$$\Delta P_{\text{sCu}} = \Delta P_{\text{U}} + \Delta P_{\text{V}} + \Delta P_{\text{W}} \tag{4.7}$$

Another step for the electromagnetic efficiency determination was calculating the machine's core losses. Those losses are calculated separately for stator and rotor using the same equation (4.8), which is used at JKU to determine core losses after exporting values of coefficients and exponents to the data pack. The only difference is in coefficients and exponents loaded from the data pack. However, since the direct current powers the rotor winding, rotor core losses have a minority share in the total core losses.

$$\Delta P_{\text{Fe}} = C_0 \cdot f_{\text{el}}^{e_0} + C_1 \cdot f_{\text{el}}^{e_1} \tag{4.8}$$

Determination of the electromagnetic efficiency also requires the input power of the machine, which is different for the motor and generator modes. In motor mode, the machine takes the input power from the supply network or inverter, but in generator mode, the input power is represented by shaft power, calculated in equation (4.9).

$$P_{\text{shaft}} = T_{\text{e}} \cdot \omega_{\text{m}} \tag{4.9}$$

As mentioned earlier, the supply voltage values are not part of the data file, so the input power for the motor mode efficiency calculation was determined by the sum of the shaft power and all losses in the machine.

$$P_{\text{el}} = P_{\text{shaft}} + \Delta P_{\text{sCu}} + \Delta P_{\text{rCu}} + \Delta P_{\text{Fe}} \tag{4.10}$$

As the machine can operate in two modes, the efficiency was calculated for both. Actual machine mode was recognized by a sign of P_{shaft}. If the value of shaft power was greater than zero, the machine was in motor mode, and efficiency was calculated using equation (4.11).

$$\eta_{\text{m}} = \frac{P_{\text{shaft}}}{P_{\text{el}}} \tag{4.11}$$

If the value of P_{shaft} was lower than zero, the machine was in generator mode, and the efficiency was calculated using equation 4.12. In this situation, the losses in the excitation winding and shaft power are taken as input power because the field current needs to be fed into the rotor to generate electric power. The output power was calculated by subtracting the remaining machine losses from the shaft power.

$$\eta_{\text{g}} = \frac{|P_{\text{shaft}}| - \Delta P_{\text{sCu}} - \Delta P_{\text{Fe}}}{|P_{\text{shaft}}| + \Delta P_{\text{rCu}}} \tag{4.12}$$

As in the case of plotting the graphs of torques versus different currents in Fig. 4.5, it was necessary to use three plots for the efficiency characteristics, which were plotted in the fourth variable, where the highest efficiency values were obtained.
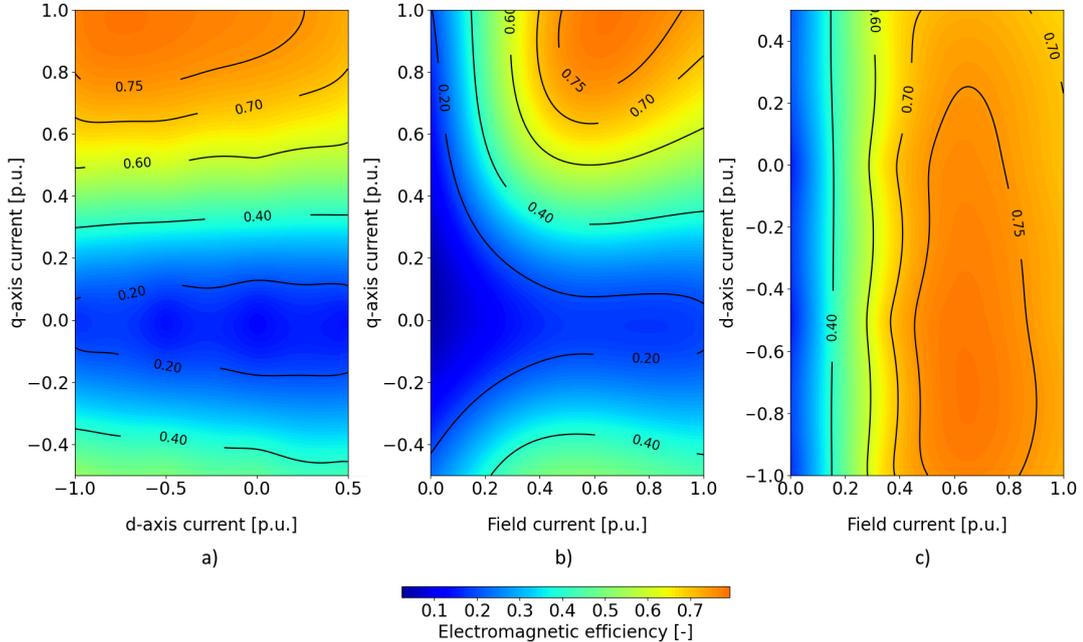
Fig. 4.5: Graphical dependence of the training data electromagnetic efficiency on a) d- and q-axis, b) Field and q-axis, c) Field and d-axis current.

The boundary between the motor and generator modes is clearly visible In Fig. 4.5 (a), (b), it is located at zero value on the q-axis of the current. In Fig. 4.5 c), on the other hand, this boundary is not visible. The efficiency drop around zero excitation current is caused by a dramatic reduction in machine torque since the machine is not excited at this area, and only remanent induction contributes to torque generation. Note that these regions are shown for the values of the fourth variable where the highest efficiency was achieved, and therefore it is not possible to show them all.

As can be noticed in this figure, the generator mode is represented in a small part of the data file, and the maximum magnitude of the torque achieved is also very low. Since the data were generated from a machine model that was not designed for the purpose of subsequent production but only as a data source to build the Python code, the exported data pack was limited in generator mode. So new data were generated from the model of a wound-rotor synchronous machine, which was designed at the Institute of Electric Drives and Power Electronics at JKU.

One of the goals of this work was to find the optimal combination of supply currents to achieve maximum efficiency. Thus, a function was integrated into a Python program to find the maximum efficiency in the efficiency matrix and generate the corresponding combination of input currents that achieved this efficiency. The values of the individual currents, together with the value of the maximum electromagnetic efficiency, are listed in Tab. 4.2 in both relative and absolute units. In the case of the training data, combined with the electromagnetic efficiency plots in Fig. 4.5, it can be concluded that the highest efficiency was obtained in the motor mode, and its value was 78.99 %. This value is relatively low, which is due to the fact that this data were generated only for the construction of the Python code, as described above. Looking at Fig. 4.4, it could be expected that the highest efficiency would be reached at just around 0.6 p.u. of the field current. Because from this value onwards, the machine's torque increases quite slowly, but as the current in the winding increases, the Joule losses in the winding increase quadratically, thus decreasing the efficiency. This hypothesis is confirmed in Fig. 4.5 and by the fact that the highest efficiency was achieved at 0.63 p.u. of the field current.

Tab. 4.2: Maximum efficiency current combination for training data.

Parameter	[p.u.]	[A]
Field current	0.63	157.45
d-axis current	-0.73	-17.21
q-axis current	0.95	45.01
Maximum efficiency	78.99 %	

5 Machine analysis

This chapter is devoted to introducing the new data to be analyzed and completing the script for the machine analysis. In order to validate the developed script, a machine designed at the Institute of Electric Drives and Power Electronics at JKU in Linz will be analyzed. This wound rotor synchronous machine can produce a maximum torque of 105.85 Nm based on simulation results. Further parameters of this machine cannot be published in this paper to avoid JKU and LCM research data leakage. The results of the analysis are presented and discussed.

5.1 Analyzed data

The format of this data set is the same as the training data set format. The individual points were simulated using the FEM method and the results of these simulations were continuously stored in one file. In this case, 49 load points were simulated and are depicted in Fig. 5.1. Also, as in the case of training data, the simulations were performed as a function of the rotation angle, so they are independent of the speed. Therefore the same speed of 6000 rpm was chosen. As can be seen from the values of the simulated currents compared with Fig. 4.2, this is a significantly more powerful machine.
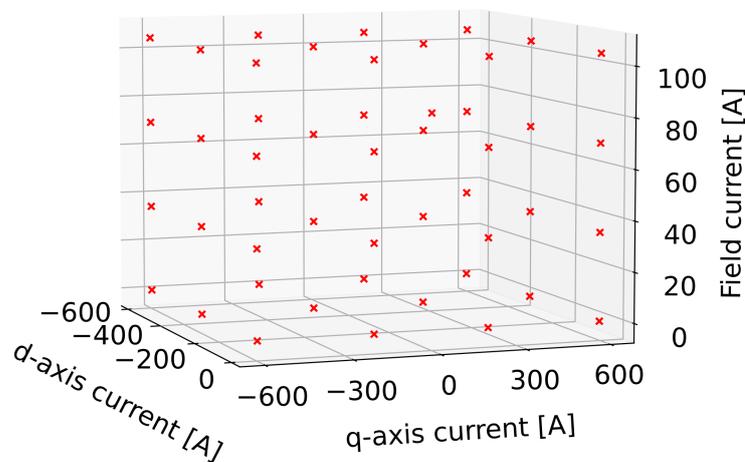
Fig. 5.1: Graphical representation of the analyzed data currents in the 3D space.

As in the previous case, different combinations of input currents under different shaft loads were simulated. The maximum values of these currents are summarized in Tab. 5.1, and these values have been used as a reference in the calculation of the per-unit values. Since only negative d-axis current was simulated, 597.66 A, the absolute value of the minimum current, was used as a reference.

Tab. 5.1: Analyzed data current values.

Parameter	Values			
Field current [A]	0	34.85	69.70	104.55
d-axis current [A]	0	-298.83	-597.66	-
q-axis current [A]	0	199.22	597.66	-

As indicated in Tab. 5.1 and Fig. 5.1, load points with the symmetrically distributed current in the q-axis, and negative current in the d-axis were calculated for the four excitation current values in the FEM simulations.

5.2   Torque characteristics

The torque characteristics were created in the same way as for the test data and must be displayed for different combinations of input currents as they can not be printed in 4D space. Fig. 5.2 shows the dependence of the machine torque on different combinations of input currents.
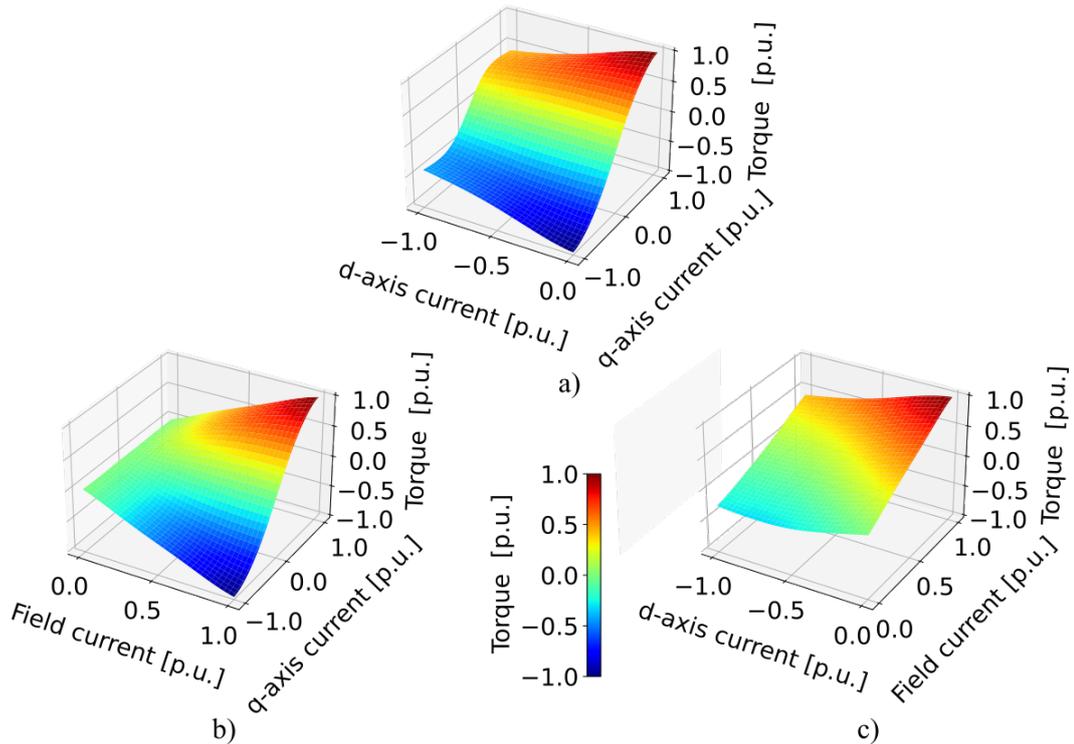
Fig. 5.2: Graphical dependence of the analyzed torque values on a) d- and q-axis, b) Field and q-axis, c) Field and d-axis current.

Compared to Fig. 4.4, an extended torque range to negative values can be seen, so there are more simulated points in the generator mode. It can also be noticed that the individual characteristics in Fig. 4.4 have a slightly different shapes. This difference may be caused by the size of the machine and its design. In both modes, a maximum torque of 105.85 Nm is achieved. This torque value was used as a reference in the calculation of the per-unit values, as in the case of the training data set.

5.3   Electromagnetic efficiency results

The most important output of this program is the determination of the dependence of the electromagnetic efficiency on different combinations of input currents and the subsequent estimation of the highest efficiency and the corresponding currents. Thus, in this section of the thesis, the analysis results in terms of efficiency are presented and discussed.
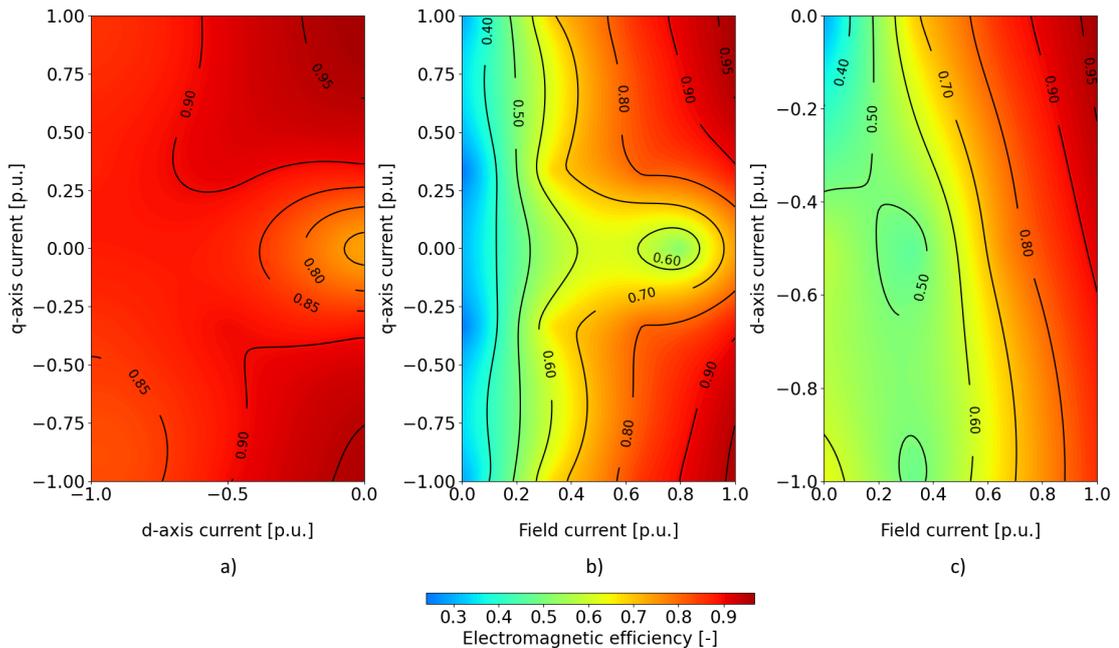
Fig. 5.3: Graphical dependence of the analyzed data electromagnetic efficiency on a) d- and q-axis, b) Field and q-axis, c) Field and d-axis current.

The machine efficiency characteristic for different input current combinations are plotted in Fig. 5.3. The characteristics in Fig. 5.3 a) and c) show that the influence of the d-axis current on the machine efficiency is not so dramatic, and the highest electromagnetic efficiency is achieved around the zero value of the d-axis current.

On the other hand, the efficiency varies with the q-axis current adjustment. As can be seen in Fig. 5.2, when the q-axis current exceeds zero value, the machine mode changes from the motor to the generator mode. The influence of the field current on the machine efficiency is shown in Fig. 5.3 b) and c). The machine's efficiency is very low for the area under 0.4 p.u. of the field current, and after passing this boundary, the efficiency fastly rises. Because the highest efficiency was achieved in the highest excitation current, this value is optimal for the machine compared to the training data, where the highest excitation current occurred with high Joule losses in the rotor winding and decreased the efficiency. The value of the d-axis current in Tab. 5.2 could also be expected because the highest torque value was obtained around the zero value of the d-axis current. The combination of mentioned currents led to the highest efficiency, 96.58 %.

Tab. 5.2: Maximum efficiency current combination for analysed data.

Parameter	[p.u.]	[A]
Field current	1.00	104.55
d-axis current	$1.83 \cdot 10^{-5}$	0.01
q-axis current	0.98	585.71
Maximum efficiency	96.58 %	

The resulting maximum efficiency is relatively high, which may be caused by the fact that it is an electromagnetic efficiency where mechanical and additional losses of the machine are not considered, and also because there is some interleaving error with RBF. This error occurs if the source point network is too sparse, and since it is a wound rotor machine, there is an additional variable in the form of the excitation winding current compared to the analysis of, for example, a permanent magnet synchronous machine, which was done in [40]. If the same amount of FEM simulations were kept for both machines, the resulting grid for analysis would be much denser for the synchronous machine with PM since here, only the 2D interpolation. The exact number of FEM simulations results in a thinner grid when interpolating in 3D space. Then the interpolation needs some extra smoothing, which reduces the accuracy of this method.

Conclusion

This thesis deals with the wound-rotor synchronous machine as an electric vehicle drive. In the first chapter, the literature research on machine types that are possible to drive an electric vehicle found five options. The construction and working principle of each machine type was described, and the advantages and disadvantages of traction application were summarized. The first one was the DC machine type, which is suitable thanks to its easy regulation, but the commutator brings many disadvantages, so it is not currently used in electric cars. The second one was the permanent magnet AC machine. This machine is widely used in electric vehicles thanks to its high efficiency and torque. The increasing cost of rare-earth materials is a disadvantage of this machine, so there is pressure to find some permanent magnet-free machines. Switched reluctance machine is the simplest one in terms of constructing a permanent magnets-free machine. It also has a disadvantage in high torque ripple and acoustic noise, but the development of this machine as a traction motor goes straight forward. The following well-known machine is the induction machine. This machine type offers a simple, robust, and low-cost option for electric vehicle drive. Due to the rotor aluminum winding and the required magnetization current, this machine achieves lower efficiency than the PM machine. However, it is used in Tesla cars, where the development of this machine type is at a high level.

The last applicable machine type is a wound rotor synchronous machine. A more detailed focus was given to this machine construction and traction application usage. The most significant advantage of this machine type is the possibility of the field current control. This possibility enables it to operate at a power factor equal to one across the whole speed range. The brushed synchronous machine provides higher starting and low-speed torque compared to the PM machine. The application in Renault electric cars was investigated.

As part of literature research on wound-rotor synchronous machines for traction applications, the modifications being made for this application were described in this thesis. Thus, the vernier machine and its working principle have been described within the scope of this thesis. Furthermore, two methods of non-contact energy transfer to the rotor winding were discussed. The first one was the rotary transformer which uses a core made of composite materials, which significantly reduces its volume. Subsequently, the concept of capacitive power transfer was introduced, whose most prominent advantage is its minimal volume. The last modification introduced was the use of hairpin windings together with stator winding rectangular-shaped conductors.

The next chapter described a wound-rotor synchronous machine model using equivalent circuits in the direct and quadrature axes. Mathematical equations were

written down from these equivalent circuits to model the machine. Within the mathematical description, the equation for the torque calculation was also given, explaining the meaning of each part of this equation. A vector diagram in motor mode was also included and explained to complete the machine description.

The fourth chapter was devoted to the transformation of the output values of the FEM simulations from the three-phase system to the rotor reference frame. Furthermore, the cooperation with JKU in Linz, from which training data for analyzing a wound-rotor synchronous machine was supplied, was described. Based on this data, a Python script was then developed to analyze the operating characteristics of this type of machine. This analysis described the methodology for evaluating the efficiency based on the provided data set. Partial results in the form of torque and efficiency characteristics were graphically presented and described.

The last chapter then dealt with the validation of the built Python script in the analysis of a wound-field synchronous machine with, which was designed at the Institute of Electric Drives and Power Electronics at JKU in Linz. The resulting torque and efficiency characteristics are discussed. Also, the maximum efficiency of the machine and the supply currents by which this efficiency was achieved were found using a Python script. These currents can then be used in the control of the machine to power it in terms of efficiency optimally. Since this data package had a relatively sparse network of FEM simulated points from the analysis, additional smoothing of the radial basis function had to be applied, which caused a slight deviation in the efficiency values. However, this deviation is not very significant and would be almost negligible with denser source data load points.

The further goals of the following thesis could be to extend the capabilities of the script for machine analysis and its subsequent use in designing a wound-field synchronous machine as a traction drive.

Bibliography

[1] LIPO, Thomas Anthony and Zhentao Stephen DU. Synchronous motor drives-a forgotten option. In: *2015 Intl Aegean Conference on Electrical Machines & Power Electronics (ACEMP), 2015 Intl Conference on Optimization of Electrical & Electronic Equipment (OPTIM) & 2015 Intl Symposium on Advanced Electromechanical Motion Systems (ELECTROMOTION)* [online]. IEEE, 2015, 2015, p. 1-5 [cit. 2021-03-31]. ISBN 978-1-4673-7239-8. Available at: doi:10.1109/OPTIM.2015.7426740

[2] WANG, Zhikun, Tze Wood CHING, Shaojia HUANG, Hongtao WANG and Tao XU. Challenges Faced by Electric Vehicle Motors and Their Solutions. *IEEE Access* [online]. 2021, **9**, 5228-5249 [cit. 2021-04-11]. ISSN 2169-3536. Available at: doi:10.1109/ACCESS.2020.3045716

[3] DE SANTIAGO, Juan, Hans BERNHOFF, Boel EKERGÅRD, Sandra ERIKSSON, Senad FERHATOVIC, Rafael WATERS and Mats LEIJON. Electrical Motor Drivelines in Commercial All-Electric Vehicles: A Review. *IEEE Transactions on Vehicular Technology* [online]. 2012, **61**(2), p. 475-484 [cit. 2021-03-31]. ISSN 0018-9545. Available at: doi:10.1109/TVT.2011.2177873

[4] SOKOLOV, Emil. Comparative study of electric car traction motors. In: *2017 15th International Conference on Electrical Machines, Drives and Power Systems (ELMA)* [online]. IEEE, 2017, 2017 p. 348-353 [cit. 2021-04-13]. ISBN 978-1-5090-6690-2. Available at: doi:10.1109/ELMA.2017.7955461

[5] VIJAYKUMAR, Lekkala, T. SELVATHAI and Rajaseeli REGINALD. Design Study on Traction Motors for Hybrid Electric Vehicle Applications. In: *2019 Innovations in Power and Advanced Computing Technologies (i-PACT)* [online]. IEEE, 2019, 2019, p. 1-6 [cit. 2021-04-13]. ISBN 978-1-5386-8190-9. Available at: doi:10.1109/i-PACT44901.2019.8960147

[6] YILDIRIM, Merve, Mehmet POLAT and Hasan KURUM. A survey on comparison of electric motor types and drives used for electric vehicles. In: *2014 16th International Power Electronics and Motion Control Conference and Exposition* [online]. IEEE, 2014, 2014, p. 218-223 [cit. 2021-04-13]. ISBN 978-1-4799-2060-0. Available at: doi:10.1109/EPEPEMC.2014.6980715

[7] SEN, Paresh Chandra. *Principles of Electric Machines and Power Electronics.* 3. Hoboken: John Wiley & Sons, 2014. ISBN 978-1-118-07887-7.

[8] FINKEN, Thomas, Matthias FELDEN and Kay HAMEYER. Comparison and design of different electrical machine types regarding their applicability in hybrid electrical vehicles. In: *2008 18th International Conference on Electrical Machines* [online]. IEEE, 2008, 2008, p. 1-5 [cit. 2021-04-14]. ISBN 978-1-4244-1735-3. Available at: doi:10.1109/ICELMACH.2008.4800044

[9] CHERNYSHEV, A. D., T. A. LISOVSKAYA and R. A. LISOVSKIY. Comparative analysis of different electrical motor types as a traction drive part in electrical transmission. In: *2017 International Conference on Industrial Engineering, Applications and Manufacturing (ICIEAM)* [online]. IEEE, 2017, 2017, p. 1-5 [cit. 2021-04-14]. ISBN 978-1-5090-5648-4. Available at: doi:10.1109/ICIEAM.2017.8076311

[10] PYRHONEN, Juha, Tapani JOKINEN and Valeria HRABOVCOVÁ. *Design of rotating electrical machines.* Second edition. Chichester, West Sussex, United Kingdom: Wiley, 2014. ISBN 9781118581575.

[11] YANG, Zhi, Fei SHANG, Ian P. BROWN and Mahesh KRISHNAMURTHY. Comparative Study of Interior Permanent Magnet, Induction, and Switched Reluctance Motor Drives for EV and HEV Applications. *IEEE Transactions on Transportation Electrification* [online]. 2015, **1**(3), 245-254 [cit. 2021-04-23]. ISSN 2332-7782. Available at: doi:10.1109/TTE.2015.2470092

[12] UN-NOOR, Fuad, Sanjeevikumar PADMANABAN, Lucian MIHET-POPA, Mohammad MOLLAH and Eklas HOSSAIN. A Comprehensive Study of Key Electric Vehicle (EV) Components, Technologies, Challenges, Impacts, and Future Direction of Development. *Energies* [online]. 2017, **10**(8) [cit. 2021-04-23]. ISSN 1996-1073. Available at: doi:10.3390/en10081217

[13] BURRESS, Tim. *Complete design/packaging assessments and operational characteristics/performance evaluations of 2012 Nissan LEAF® inverter/motor and 2012 Hyundai Sonata inverter/hybrid starter-generator (HSG): 2013 U.S. DOE Hydrogen and Fuel Cells Program and Vehicle Technologies Program Annual Merit Review and Peer Evaluation Meeting.* Oak ridge: Oak Ridge National Laboratory, 2013.

[14] WILLIAMSON, Sheldon S., Srdjan M. LUKIC and Ali EMADI. Comprehensive drive train efficiency analysis of hybrid electric and fuel cell vehicles based on motor-controller efficiency modeling. *IEEE Transactions on Power Electronics* [online]. 2006, **21**(3), 730-740 [cit. 2021-04-23]. ISSN 0885-8993. Available at: doi:10.1109/TPEL.2006.872388

[15] HAGHBIN, Saeid, Ali RABIEI and Emma GRUNDITZ. Switched reluctance motor in electric or hybrid vehicle applications: A status review. In: *2013 IEEE 8th Conference on Industrial Electronics and Applications (ICIEA)* [online]. IEEE, 2013, 2013, p. 1017-1022 [cit. 2021-04-23]. ISBN 978-1-4673-6322-8. Available at: doi:10.1109/ICIEA.2013.6566516

[16] THOMAS, Robin, Lauric GARBUIO, Laurent GERBAUD and Hervé CHAZAL. Modeling and design analysis of the Tesla Model S induction motor. In: *2020 International Conference on Electrical Machines (ICEM)* [online]. Gothenburg, 2020, 2020-12-01, p. 495—501 [cit. 2021-04-14]. ISBN 978-1-7281-9945-0. Available at: doi:10.1109/ICEM49940.2020.9270646

[17] TINTELECAN, Adriana, Anca Constantinescu - DOBRA and Claudia MARTIS. Life Cycle Assessment Comparison of Synchronous Motor and Permanent Magnet Synchronous Motor. In: *2020 International Conference and Exposition on Electrical And Power Engineering (EPE)* [online]. IEEE, 2020, 2020-10-22, p. 205-210 [cit. 2021-04-19]. ISBN 978-1-7281-8126-4. Available at: doi:10.1109/EPE50722.2020.9305636

[18] ROSSI, Claudio, Domenico CASADEI, Alessio PILATI and Matteo MARANO. Wound Rotor Salient Pole Synchronous Machine Drive for Electric Traction. In: *Conference Record of the 2006 IEEE Industry Applications Conference Forty-First IAS Annual Meeting* [online]. IEEE, 2006, 2006, p. 1235-1241 [cit. 2021-04-23]. ISBN 1-4244-0364-2. ISSN 0197-2618. Available at: doi:10.1109/IAS.2006.256689

[19] DOPPELBAUER, Martin and Patrick WINZER. A lighter motor for tomorrow's electric car. *IEEE Spectrum* [online]. 2017, **54**(7), 26-31 [cit. 2021-03-31]. ISSN 0018-9235. Available at: doi:10.1109/MSPEC.2017.7951719

[20] KANE, Mark. Renault Electric Motor Production at Cléon - Photos & Videos. In: *INSIDEEVs* [online]. Miami, 2015 [cit. 2021-05-01]. Available at: https://insideevs.com/news/327111/renault-electric-motor-production-at-cleon-photos-amp-videos/

[21] TAN, Jonathan James. Renault Zoe-s new electric motor to be built at Cléon. In: *Paultan* [online]. Selangor, 19. 06. 2015 [cit. 2021-05-04]. Available at: https://paultan.org/2015/06/19/renault-zoe-new-electric-motor-cleon-plant/

[22] KOPYLOV, Igor Petrovič. *Stavba elektrických strojů*. 1. Praha: SNTL, 1988.

[23] TOBA, Akio and Thomas Anthony LIPO. Generic torque-maximizing design methodology of surface permanent-magnet vernier machine. In: *IEEE Transactions on Industry Applications* [online]. IEEE, 2000, Dec 2000, 1539 - 1546 [cit. 2021-11-11]. ISSN 1939-9367. Available at: doi:10.1109/28.887204

[24] BALOCH, Noman and Byung-il KWON. A Distributed Winding Wound Field Pole-Changing Vernier Machine for Variable Speed Application. *IEEE Transactions on Magnetics* [online]. 2019, **55**(7), 1-6 [cit. 2021-11-12]. ISSN 0018-9464. Available at: doi:10.1109/TMAG.2019.2900470

[25] BORTIS, Dominik, Lukas FASSLER, Andreas LOOSER and Johann W. KOLAR. Analysis of rotary transformer concepts for high-speed applications. In: *2013 Twenty-Eighth Annual IEEE Applied Power Electronics Conference and Exposition (APEC)* [online]. Long Beach, CA, USA: IEEE, 2013, 2013, p. 3262-3269 [cit. 2021-11-14]. ISBN 978-1-4673-4355-8. ISSN 1048-2334. Available at: doi:10.1109/APEC.2013.6520768

[26] DI GIOIA, Antonio, Ian P. BROWN, Yue NIE, Ryan KNIPPEL, Daniel C. LUDOIS, Jiejian DAI, Skyler HAGEN and Christian ALTEHELD. Design and Demonstration of a Wound Field Synchronous Machine for Electric Vehicle Traction With Brushless Capacitive Field Excitation. *IEEE Transactions on Industry Applications* [online]. 2018, **54**(2), 1390-1403 [cit. 2021-11-15]. ISSN 0093-9994. Available at: doi:10.1109/TIA.2017.2784799

[27] DI GIOIA, Antonio, Ian P. BROWN, Yue NIE, Ryan KNIPPEL, Daniel C. LUDOIS, Jiejian DAI, Skyler HAGEN and Christian ALTEHELD. Design of a wound field synchronous machine for electric vehicle traction with brushless capacitive field excitation. In: *2016 IEEE Energy Conversion Congress and Exposition (ECCE)* [online]. IEEE, 2016, 2016, p. 1-8 [cit. 2021-11-15]. ISBN 978-1-5090-0737-0. Available at: doi:10.1109/ECCE.2016.7855023

[28] RAMINOSOA, Tsarafidy and Randy WILES. Contactless Rotor Excitation for Traction Motors. In: *2018 IEEE Energy Conversion Congress and Exposition (ECCE)* [online]. IEEE, 2018, 2018, p. 6448-6453 [cit. 2021-11-14]. ISBN 978-1-4799-7312-5. Available at: doi:10.1109/ECCE.2018.8557553

[29] LUDOIS, Daniel C., Justin K. REED and Kyle HANSON. Capacitive Power Transfer for Rotor Field Current in Synchronous Machines. *IEEE Transactions on Power Electronics* [online]. 2012, **27**(11), 4638-4645 [cit. 2021-11-15]. ISSN 0885-8993. Available at: doi:10.1109/TPEL.2012.2191160

[30] LUDOIS, Daniel C. *Brushless and Permanent Magnet Free Wound Field Synchronous Motors for EV Traction* [online]. University of Wisconsin: Madison Illinois Institute of Technology, 2017 [cit. 2021-11-15]. Available at: https://www.osti.gov/servlets/purl/1349258

[31] JUNG, Dae-Sung, Yong-Ho KIM, Un-Ho LEE and Hyeoun-Dong LEE. Optimum Design of the Electric Vehicle Traction Motor Using the Hairpin Winding. In: *2012 IEEE 75th Vehicular Technology Conference (VTC Spring)* [online]. IEEE, 2012, 2012, p. 1-4 [cit. 2021-11-23]. ISBN 978-1-4673-0990-5. Available at: doi:10.1109/VETECS.2012.6240320

[32] PARK, Hyeon-Jin and Myung-Seop LIM. Design of High Power Density and High Efficiency Wound-Field Synchronous Motor for Electric Vehicle Traction. *IEEE Access* [online]. 2019, **7**, 46677-46685 [cit. 2021-11-24]. ISSN 2169-3536. Available at: doi:10.1109/ACCESS.2019.2907800

[33] PARK, Min-Ro, Dong-Min KIM, Young-Hoon JUNG, Myung-Seop LIM and Jung-Pyo HONG. Modeling, Design and Control of Wound-Field Synchronous Motor for High Energy Efficiency of Electric Vehicle. In: *2019 IEEE Energy Conversion Congress and Exposition (ECCE)* [online]. IEEE, 2019, 2019, p. 3960-3967 [cit. 2021-11-24]. ISBN 978-1-7281-0395-2. Available at: doi:10.1109/ECCE.2019.8912279

[34] PYRHÖNEN, Juha, Valeria HRABOVCOVÁ and Scott SEMKEN. *Electrical machine drives control: an introduction.* Chichester, West Sussex, United Kingdom: John Wiley & Sons, [2016]. ISBN 9781119260455.

[35] MA, Yiming, Jin WANG, Yang XIAO, Libing ZHOU and Zi-Qiang ZHU. Two-Level Surrogate-Assisted Transient Parameters Design Optimization of a Wound-Field Synchronous Machine. *IEEE Transactions on Energy Conversion* [online]. 03 September 2021, **2021**, 1-1 [cit. 2021-12-06]. ISSN 0885-8969. Available at: doi:10.1109/TEC.2021.3110095

[36] WISNIEWSKI, Teodor, Jean-Claude VANNIER, Bruno LORCET, Jacques SAINT-MICHEL and Xavier JANNOT. Extended dq modeling of wound-rotor synchronous machines with dampers for transient analysis. In: *2017 18th International Symposium on Electromagnetic Fields in Mechatronics, Electrical and Electronic Engineering (ISEF) Book of Abstracts* [online]. IEEE, 2017, 2017, p. 1-2 [cit. 2021-12-16]. ISBN 978-1-5386-1661-1. Available at: doi:10.1109/ISEF.2017.8090768

[37] BACHEV, Ivan, Ludmil STOYANOV, Vladislav PETROV and Emilia HADJIATANASOVA-DELEVA. Application of Synchronous Machines- Models for Distance Learning Purposes. In: *2021 17th Conference on Electrical Machines, Drives and Power Systems (ELMA)* [online]. IEEE, 2021, 2021-7-1, p. 1-5 [cit. 2021-12-16]. ISBN 978-1-6654-3582-6. Available at: doi:10.1109/ELMA52514.2021.9503005

[38] GARSHELIS, Ivan J. and Stijn P.L. TOLLENS. Influence of geometric factors on the polarity of a remanent magnetization. *IEEE Transactions on Magnetics* [online]. 2005, **41**(10), 2796-2798 [cit. 2022-04-06]. ISSN 0018-9464. Available at: doi:10.1109/TMAG.2005.854772

[39] SKALA, Vaclav. Fast Interpolation and Approximation of Scattered Multidimensional and Dynamic Data Using Radial Basis Functions. In: *WSEAS Transactions on Mathematics* [online]. 2013, 2013, p. 501-511 [cit. 2022-05-07]. ISSN 2224-2880. Available at: http://afrodita.zcu.cz/ skala/PUBL/PUBL_2013/2013_RBF-Scattered.pdf

[40] WEIDENHOLZER, Guenther, Siegfried SILBER, Gerald JUNGMAYR, Gerd BRAMERDORFER, Herbert GRABNER and Wolfgang AMRHEIN. A flux-based PMSM motor model using RBF interpolation for time-stepping simulations. In: *2013 International Electric Machines & Drives Conference* [online]. IEEE, 2013, 2013, p. 1418-1423 [cit. 2022-04-07]. ISBN 978-1-4673-4974-1. Available at: doi:10.1109/IEMDC.2013.6556323

Symbols and abbreviations

AC   Alternating Current

CPC   Capacitive Power Coupler

DC   Direct Current

EV   Electric Vehicle

EMF   Electromotive Force

FEM   Finite Element Method

FOC   Field-Oriented Control

HEV   Hybrid Electric Vehicle

IGBT   Insulated Gate Bipolar Transistor

IM   Induction Motor

IPM   Interior Permanent Magnet¨

JKU   Johannes Kepler University

LCM   Linz Center of Mechatronics

MTPA   Maximum Torque Per Ampere

PM   Permanent Magnet

RMS   Root Mean Square

RBF   Radial Basis Function

SB   Synchronous Brushed

SM   Synchronous Machine

SPSM   Salient Pole Synchronous Machine

SRM   Switched Reluctance Motor

WR   Wound Rotor

WFSM   Wound Field Synchronous Machine

A surface area [m²]

A_{cond}	conductor cross-section area [m^2]
C	capacitance [F]
$C_{0/1}$	Iron loss coefficient [-]
$\hat{e_m}$	back electromotive force vector induced by the air gap flux linkage [V]
$\hat{e_{mf}}$	back electromotive force vector induced by the rotor flux linkage [V]
$\hat{e_s}$	back electromotive force vector induced by the stator flux linkage [V]
$e_{0/1}$	Iron loss exponent [-]
f	frequency [Hz]
g	air gap length [m]
h_{ec}	end coil height [m]
I_{f}	field current [A]
I_{s}	stator phase current [A]
i_{d}	direct axis current [A]
i_{f}	field current [A]
i_{q}	quadrature axis current [A]
$\hat{i_{\text{s}}}$	stator current space vector [A]
i_{sU}	stator current in phase U [A]
i_{sV}	stator current in phase V [A]
i_{sW}	stator current in phase W [A]
L_{D}	total direct axis inductance of the damper winding [H]
$L_{\text{D}\sigma}$	direct axis leakage inductance of the damper winding [H]
L_{d}	direct axis synchronous inductance [H]
L_{dD}	mutual inductance between the direct axis stator and damper equivalent winding [H]

L_{df}	mutual inductance between the stator direct axis equivalent winding and the field winding[H]
L_{dQ}	mutual inductance between the direct axis stator equivalent winding and the quadrature axis equivalent damper winding [H]
L_{f}	field winding inductance [H]
$L_{\mathrm{f}\sigma}$	field winding leakage inductance [H]
L_{fD}	mutual inductance between the field winding and the direct axis equivalent damper winding[H]
$L_{\mathrm{k}\sigma}$	Cannay inductance parameter [H]
L_{md}	direct axis magnetizing inductance [H]
L_{mq}	quadrature axis magnetizing inductance [H]
L_{q}	quadrature axis synchronous inductance [H]
L_{Q}	total quadrature axis inductance of the damper winding [H]
$L_{\mathrm{Q}\sigma}$	quadrature axis leakage inductance of the damper winding [H]
L_{qQ}	mutual inductance between the quadrature axis stator and damper equivalent winding [H]
L_{stk}	core stack length [m]
$L_{\mathrm{s}\sigma}$	stator leakage inductance [H]
N_{f}	number of turns in the field winding [-]
N_{ph}	number of turns in series per phase [-]
N_{s}	number of stator slots [-]
P_{el}	theoretical electrical power [W]
P_{shaft}	power on the shaft [W]
p	number of armature pole pairs [-]
p_{r}	number of rotor pole pairs [-]
ΔP	losses [W]
ΔP_{Fe}	iron losses [W]

ΔP_{rCu}	Joule losses in field winding [W]
ΔP_{ph}	Joule losses in one stator phase [W]
ΔP_{sCu}	]total stator Joule losses [W]
ΔP_{U}	Joule losses in stator phase U [W]
ΔP_{V}	Joule losses in stator phase V [W]
ΔP_{W}	Joule losses in stator phase W [W]
R_{D}	resistance of one the direct axis damper winding [Ω]
R_{f}	resistance of the field winding [Ω]
R_{Q}	resistance of one the quadrature axis damper winding [Ω]
R_{s}	resistance of one phase of the stator winding [Ω]
r_{f}	field coil conductor radius [m^2]
T	temperature [°C]
T_{e}	electromagnetic torque [Nm]
U_{s}	stator voltage [V]
u_{d}	direct axis component of stator voltage [V]
u_{f}	field winding voltage [V]
u_{q}	quadrature axis component of stator voltage [V]
$\hat{u}_{\mathrm{s}}$	stator voltage space vector [V]
α	resistivity temperature coefficient [K^{-1}]
δ	skin depth [mm]
ε	permitivity [Fm^{-1}]
η_{m}	efficiency in motor mode [-]
η_{g}	efficiency in generator mode [-]
θ_{r}	rotor angle [rad]
μ_0	vacuum permeability [Hm^{-1}]

μ_r	vacuum permeability [Hm^{-1}]
π	mathematical constant [-]
ρ_C	electrical resistivity of copper [Ωm]
σ	electrical conductivity [Sm^{-1}]
τ_f	average field coil span [m]
τ_s	average stator coil span [m]
ϕ_r	rotor magnetic flux [Wb]
ψ_D	direct axis component of damper flux linkage [Vs]
ψ_d	direct axis component of stator flux linkage [Vs]
ψ_f	field winding flux linkage [Vs]
ψ_Q	quadrature axis component of damper flux linkage [Vs]
ψ_q	quadrature axis component of stator flux linkage [Vs]
$\hat{\psi}_\mathrm{m}$	air gap flux linkage space vector [Vs]
$\hat{\psi}_\mathrm{s}$	stator flux linkage space vector [Vs]
ψ_U	flux linkage of phase U [Vs]
ψ_V	flux linkage of phase V [Vs]
ψ_W	flux linkage of phase W [Vs]
ω_r	rotor angular velocity [rads^{-1}]